

The Origin and Kinematics of Cold Gas in Galactic Winds: Insight from Numerical Simulations

Akimi Fujita^{1,2}, Crystal L. Martin^{1,a,b}, Mordecai-Mark Mac Low^{3,2,4}, Kimberly C. B. New⁵,
and Robert Weaver⁵

¹*Department of Physics, University of California, Santa Barbara, CA 93106;
cmartin@physics.ucsb.edu*

²*Max Planck Institute of Astronomy, D-69117 Heidelberg, Germany*

³*Department of Astrophysics, American Museum of Natural History, New York, NY,
10024; mordecai@amnh.org*

⁴*Institut der Theoretische Astrophysik, Zentrum für Astronomie der Universität Heidelberg,
D-69120 Heidelberg, Germany*

⁵*Los Alamos National Laboratory, Los Alamos, NM, 87545*

^a*Packard Fellow*

^b*Alfred P. Sloan Foundation Fellow*

ABSTRACT

We study the origin of Na I absorbing gas in ultraluminous infrared galaxies motivated by the recent observations by Martin of extremely superthermal linewidths in this cool gas. We model the effects of repeated supernova explosions driving supershells in the central regions of molecular disks with $M_d = 10^{10} M_\odot$, using cylindrically symmetric gas dynamical simulations run with ZEUS-3D. The shocked swept-up shells quickly cool and fragment by Rayleigh-Taylor instability as they accelerate out of the dense, stratified disks. The numerical resolution of the cooling and compression at the shock fronts determines the peak shell density, and so the speed of Rayleigh-Taylor fragmentation. We identify cooled shells and shell fragments as Na I absorbing gas and study its kinematics along various sightlines across the grid. We find that simulations with a numerical resolution of ≤ 0.2 pc produce multiple Rayleigh-Taylor fragmented shells in a given line of sight that appear to explain the observed kinematics. We suggest that the observed wide Na I absorption lines, $\langle v \rangle = 320 \pm 120$ km s⁻¹ are produced by these multiple fragmented shells traveling at different velocities. We also suggest that some shell fragments can be accelerated above the observed average

terminal velocity of 750 km s^{-1} by the same energy-driven wind with an instantaneous starburst of $\sim 10^9 M_{\odot}$. The mass carried by these fragments is only a small fraction of the total shell mass, while the bulk of mass is traveling with velocities consistent with the observed average shell velocity $330 \pm 100 \text{ km s}^{-1}$. Our results show that an energy-driven bubble causing Rayleigh-Taylor instabilities can explain the kinematics of cool gas seen in the Na I observations without invoking additional physics relying primarily on momentum conservation, such as entrainment of gas by Kelvin-Helmholtz instabilities, ram pressure driving of cold clouds by a hot wind, or radiation pressure acting on dust.

Subject headings: hydrodynamics, supernovae: general, ISM: bubbles, galaxies: starburst, ISM: jets and outflows, ISM: kinematics and dynamics

1. Introduction

Nearly all starburst galaxies, regardless of mass, appear to drive large-scale gaseous outflows, or galactic winds (Heckman et al. 1990; Martin 1999). Measurements demonstrate that these metal-enriched winds transport interstellar gas and supernova ejecta into galactic halos (Martin, et al. 2002). These winds are thought to influence the thermal and chemical evolution of the intergalactic medium and hence the formation of galaxies as well as their evolution.

From radio to X-ray frequencies, observations of starburst galaxies reveal outflowing gas over a very broad temperature range (Martin et al. 2002). However, all observed emission is relatively near the galaxy, within a projected separation of about 10 kpc, due to the radial density gradient of the wind and density-squared dependence of emission processes. Absorption-line measurements are more sensitive to extended, low-density gas. The number of detections of blue-shifted (i.e. outflowing) interstellar absorption lines in starburst galaxy spectra has grown by a large factor in recent years (Heckman et al. 2000; Rupke et al. 2002; Schwartz & Martin 2004; Martin 2005). The shortcoming of absorption line measurements is that they do not uniquely determine the distance between the galaxy and the absorbing material.

Numerical simulations of galactic winds can provide needed insight into where the absorption originates. Using simulations to interpret observations, and observations to constrain simulations, is probably the only way to really understand these complex outflows dynamically. Modeling the early evolution of a galactic wind as it blows out of its disk requires a numerical, rather than analytic, approach due to the importance of nonlinear

hydrodynamic and thermal instabilities.

Supershells evolve with roughly spherical geometry until they grow to scales of the disk gas scale-height (Tomisaka & Ikeuchi 1986, 1988; Mac Low & McCray 1988; Tenorio-Tagle & Bodenheimer 1988; de Young & Heckman 1994). The acceleration of the shell into the galactic halo causes it to fragment via Rayleigh-Taylor (R-T) instabilities (Mac Low, McCray, & Norman 1989). The hot, low-density bubble interior radiates inefficiently. The wind can sweep up new shells of ambient gas, that in turn fragment by R-T instability, leaving a broad region containing fragments of fast-moving cool gas.

The swept up shell is driven by the thermal pressure of the interior $P = \rho c_s^2$, where c_s is the interior sound speed. After blowout, the hot gas expands freely through the fragmented shell, producing a supersonic, energy-driven wind with velocity v_w . Although entrained shell fragments can still be accelerated by the ram pressure of the wind $P_{ram} = \rho v_w^2$, this appears to be a minor contribution to their total kinetic energy. This can be seen by comparing the velocity of a bubble expanding into a uniform medium at a radius of one scale height to the final shell fragment velocities, as reported, for example, by Mac Low et al. (1989). These are the same, to within a factor of two.

Properties of the cool gas in starburst winds have been estimated from observations of interstellar Na I lines in starburst galaxy spectra. Estimates of the total mass of cold gas in these outflows have large uncertainties at present due to line saturation at low resolution as well as corrections for ionization state and dust depletion. Nonetheless, it has been emphasized that the momentum of the cool flows appear to be somewhat less than the amount available from either supernova ejecta or the radiation field, at least for the most luminous starbursts (Martin 2006; Rupke et al. 2005). The same approximations, however, also yield kinetic energies for the cool outflow that are only a few percent (up to a few tens of percent) of the supernova energy. The same flows could also be driven by energy-conserving bubbles, with only a small fraction of the total energy in the bubble going to accelerating the cold gas.

The standard scenario used for interpreting starburst wind absorption is based on the simulation shown in Figure 11 of Heckman et al. (2000), which suggests that dense clouds are advected into the wind at the interface between the low-latitude disk and the wind, by Kelvin-Helmholtz instability. With a grid resolution of 4.9 pc, however, the clumps of dense gas are not fully resolved in that simulation, leaving artificially large clumps that completely stop fragmenting below ~ 6 zone size. We will show below that the R-T instability is suppressed in secondary shells at that resolution, as well, substantially changing the distribution of cool gas.

We identify the location of the absorbing gas in fragmenting shells of swept-up gas, using high-resolution simulations. Although in our models we compute only up to the time of blowout because of the small region covered by our computational grid, we use the ballistic approximation (Zahnle & Mac Low 1995; Fujita et al. 2004) to show that gravitational deceleration does not act strongly on the shells and fragments during the starburst duration (10–40 Myr) if their velocities exceed $50 - 200 \text{ km s}^{-1}$ at blowout. This analysis is based, however, on an assumption that the bulk of their mass remains unablated by the wind blowing past them. Understanding the full history of shell fragments and clumps will require substantial further work.

We address the origin and kinematics of the cold wind as measured in the Na I $\lambda\lambda 5890, 96$ absorption lines. The observations pose three major questions. First, why do the absorption line widths tend to greatly exceed the thermal velocity dispersion of warm neutral gas? The average full width at half maximum (FWHM) of the dynamic component is $320 \pm 120 \text{ km s}^{-1}$ in ultraluminous infrared galaxies (ULIRGs), while the line widths range from 150 to 600 km s^{-1} in luminous infrared galaxies. Second, why do the terminal velocities of the cold gas approach the escape velocities from the starburst galaxies (Martin 2005)? Third, what do the maximum and mean velocities measured in the line profiles really represent physically?

We use our models to pursue five investigations. First, we investigate how the absorption properties change with viewing angle. We specifically test whether multiple R-T fragmented shells along a line of sight can reproduce the broad line width seen in Na I absorption lines. Second, we vary the numerical resolution to demonstrate how increased resolution of radiative cooling behind the shocks, and so of shell fragmentation, affect the results.

Third, we make a more general parameter study addressing variations in the properties of the outflowing cold gas with starburst luminosity, the size of the starburst region, and gas surface density. Fourth, we can obtain insight into the complicated dynamics of multiphase outflows, particularly their dependence on the mass-loading of the wind. We investigate mass-loading rates between $\sim 1.7 - 120 M_{\odot} \text{ yr}^{-1}$ and vary the mechanical luminosity of the starburst between $10^{41} - 10^{43} \text{ erg s}^{-1}$ to see what velocities are reached by the swept-up shells and their fragments. The observed X-ray temperatures vary little with starburst luminosity $T \sim 10^7 \text{ K}$, so the terminal wind velocities should vary little with luminosity (above some critical value required for blowout).

Finally, Heckman et al. (2000) argued that both Na I absorbing and H α emitting gas can not originate in the swept-up shells because of the lack of strong correlation between the widths of Na I absorption lines and H α emission lines. For example, the outflow sources with very broad ($400\text{--}600 \text{ km s}^{-1}$) Na I absorption lines have H α emission-line widths ranging

from 145 to 1500 km s⁻¹. Although a full nebular emission calculation is well beyond the scope of this paper, we do discuss where the ionization front might reside for various ionizing photon luminosities. We study the kinematics of the low-ionization Na I absorbing gas and photoionized H α emitting gas by separating them crudely, using the photoionization code of Abel, Norman, & Madau (1999).

The acceleration of shell fragments is sensitive to how well shell fragmentation is resolved. Applying adaptive mesh refinement (AMR) techniques to this problem can maintain high resolution in the shocked shells and clouds. This paper is the first step toward such an improved simulation. We compare the blowout problem run on a fixed grid to the same problem run with an adaptive grid, focusing on the comparison to measured properties of cold gas in galactic winds.

In this paper, we describe our disk and star formation models in § 2 and our numerical method in § 3. We give the results of our parameter studies in § 4 and discuss comparisons with observations in § 5, followed by conclusions in § 6. In an Appendix, we show the results of test simulations of blowout in a dwarf galaxy by ZEUS-3D (Stone & Norman 1992; Clarke 1994) and SAGE (SAIC’s Adaptive Grid, Eulerian hydrocode; Kerbyson et al. 2002).

2. Disk and Star Formation Models

The parameters of our starburst model are based on the properties of ULIRGs to facilitate comparison with Martin (2005, 2006). We use hydrodynamic simulations to model the effects of multiple supernova explosions in the central 200 pc \times 100 pc region of the molecular disk of a ULIRG. Our model is an extension of the blowout model in dwarf galaxies described by Mac Low & Ferrara (1999) and Fujita et al. (2003). Our fiducial numerical resolution is 0.2 pc, sufficient to resolve cooling behind the shocks, and so the fragmentation of the swept-up shells by R-T instability as well as possible within a reasonable computational time. To study the effects of numerical resolution, we use models with resolution ranging from 0.1 to 0.8 pc.

2.1. Disk

ULIRGs are starburst galaxies with infrared luminosity $> 10^{12} L_{\odot}$, and are usually found in major mergers and interacting galaxies (Sanders et al. 1988). They are believed to go through starburst phases twice, when the gas in a galaxy with a prograde orbital geometry is tidally disturbed during the first encounter with another galaxy and when both galaxies

meet again and finally merge (Murphy et al. 2001). We choose to model a molecular gas-rich spiral galaxy on its first encounter with another galaxy of similar mass.

We set up a molecular disk with $M_g = 10^{10} M_\odot$ in a dark matter halo with $M_{halo} = 5 \times 10^{12} M_\odot$. CO observations of ULIRGs at both first and second passages show the presence of molecular disks with $M_g = 0.4 - 1.5 \times 10^{10} M_\odot$, which is in the range found for molecular gas-rich spiral galaxies (Sanders et al. 1988; Solomon et al. 1997). However, the emission originates in regions a few hundred parsecs in radius, yielding surface densities of $\sim 0.5 - 1 \times 10^4 M_\odot \text{ pc}^{-2}$, within which the molecular mass dominates the dynamical mass (Sanders et al. 1988; Solomon et al. 1997). At these high surface densities, molecular hydrogen will dominate (Blitz & Rosolowsky 2006), as it can form within a few million years in turbulent regions with densities over 100 cm^{-3} (Glover & Mac Low 2007). The density of H_2 traced by CO emission is $\sim 500 \text{ cm}^{-3}$, comparable to the envelope of GMCs, while a region of much higher density in ULIRGs is traced by HCN emission, $\sim 10^5 \text{ cm}^{-3}$, comparable to star-forming cloud cores (Solomon et al. 1992a).

We assume that the entire interstellar medium (ISM) is a scaled-up version of a normal galactic disk with the ambient densities a factor of ~ 100 higher, making even the intercloud medium a molecular region. Thus we assume that the surface density distribution of the molecular disk is exponential, with $\Sigma(R) = \Sigma_0 \exp(-R/R_d)$ where R_d is a scale radius (see also $\Sigma(R)$ of Arp 220 by Scoville 1997).

We choose to model a disk with a central surface density of $\Sigma_0 = 10^4 M_\odot \text{ pc}^{-2}$, with a disk scale radius $R_d = 0.7 \text{ kpc}$. The disk is in hydrostatic equilibrium with a Navarro, Frenk, & White (1997; hereafter NFW) halo potential, and a disk potential based on the thin disk approximation (Toomre 1963), since $M_{dyn} \approx M_g$. The NFW potential is

$$\Phi(x) = \frac{GM_{halo}}{R_v} \frac{\log(1 + cx)/x}{F(c)}, \quad (1)$$

where R_v is the virial radius (326 kpc), $x = r/R_v$, c is a halo concentration factor, set to $c = 5$, appropriate for a large halo (Jimenez, Verde, & Oh 2003), and $F(c) = (\log(1 + c) - c)/(1 + c)$.

The velocity dispersion of the molecular gas is observed to be 90 km s^{-1} in Arp 220, which appears to be at the end of the merging process (Scoville 1997). Such a high velocity dispersion yields a scale height of 15 pc in its disk (Scoville et al. 1997). Molecular clouds with such high dispersion will get destroyed by colliding with other clouds, so the cooling time behind the shocks must be shorter than the destruction time interval. We assume the gas is supported by turbulence with a similarly high velocity dispersion $c_s = 55 \text{ km s}^{-1}$. It is lower than 90 km s^{-1} because gravity from our disk gas and halo can not confine the gas with a higher velocity dispersion. As a comparison, we also model a disk with a higher

surface density of $\Sigma_0 = 5 \times 10^4 \text{ M}_\odot \text{ pc}^{-2}$ with $R_d = 0.17 \text{ kpc}$ and $c_s = 90 \text{ km s}^{-1}$, based on the central surface density observed in Arp 220. This is the highest Σ_0 of all observed ULIRGs.

Figure 1 shows the vertical density distributions of both disks. The exponential scale heights are rather small, 7 and 2 pc, but the gas within them is very dense, ~ 5000 and 10^5 cm^{-3} respectively. The gas density is still $\sim 500 \text{ cm}^{-3}$ at $Z \gtrsim 4R_d$. At higher altitudes, where the gas is less dense, the gas is physically atomic or even ionized. We do not take that state change into account in our model, though. When the number density drops to $n = 10^{-2} \text{ cm}^{-3}$ we set the gas density in the halo constant as it is no longer dynamically important on the length and time scales treated in our model.

2.2. Star Formation

We assume a single starburst that occurs at the center of the disk, and that all the kinetic energy of the starburst supernovae is released in a central wind of constant mechanical luminosity. In reality, the discrete energy inputs from supernovae generate blastwaves that become subsonic in the hot interior of the bubble first produced by stellar winds, and hence can be treated as a continuous mechanical luminosity in the study of bubble dynamics (Mac Low & McCray 1988). These assumptions mean that a single superbubble forms, evolving to produce a bipolar outflow of gas.

Figure 2 shows the evolution of mechanical luminosity L_{mech} as a function of time for an instantaneous starburst with 10^9 M_\odot of gas turning into stars and for continuous starbursts with star formation rates of 100 and 500 $\text{M}_\odot \text{ yr}^{-1}$, based on the Starburst 99 model (Leitherer et al. 1999). The Starburst 99 model uses a power law initial mass function with exponent $\alpha = 2.35$ between low-mass and high-mass cutoff masses of $M_{low} = 1 \text{ M}_\odot$ and $M_{up} = 100 \text{ M}_\odot$ with solar metallicity. Star formation rates in ULIRGs are estimated to be $\gtrsim 100 \text{ M}_\odot \text{ yr}^{-1}$ based on far-infrared luminosities and the assumption of continuous star formation (see Table 1 of Martin 2005; note that the star formation rates given there correspond to a low mass cutoff of 0.1 M_\odot and must be divided by a factor of 2.55 before comparison to the population synthesis models).

The amount of mechanical power supplied per unit stellar mass depends on the star formation history. About ~ 40 million supernovae, for example, will be produced by an instantaneous starburst of $M_* = 10^9 \text{ M}_\odot$. For a continuous starburst, L_{mech} increases until the death rate of massive stars catches up to their birth rate, after about 40 Myr. The power rises particularly rapidly over the first few Myr, the period modeled by our simulation. Fig. 2a

shows the evolution for a continuous starbursts with $500 \text{ M}_\odot \text{ yr}^{-1}$ and $100 \text{ M}_\odot \text{ yr}^{-1}$. For our ULIRG models, we use constant mechanical luminosity winds with values $L_{\text{mech}} = 10^{43}$, 10^{42} , and $10^{41} \text{ erg s}^{-1}$. The highest of these corresponds to the mechanical luminosity expected from stellar winds during the first 2 Myr of an instantaneous starburst with $M_* = 10^9 \text{ M}_\odot$. The subsequent supernovae will result in a far higher mechanical luminosity, but that is likely to be vented out of the galactic disk through the hole opened by the initial blowout. $L_{\text{mech}} = 10^{43} \text{ erg s}^{-1}$ also corresponds to a model with a constant SFR of $15.9 \text{ M}_\odot \text{ yr}^{-1}$. This correspondence assumes the birth and death rates of massive stars are in equilibrium, which is achieved about 40 Myr after the burst begins. In this scenario, the burst would be ongoing through its initial stages before our simulation starts, but gas displaced by the initial feedback had been replaced by inflows, and prior feedback energy was largely radiated. Our simulation is not such a good representation of this scenario.

We note it is an oversimplification to assume a single starburst at the disk center for modeling a galactic outflow. Bipolar outflows are seen in some starburst galaxies such as M82 (Strickland et al. 2004; Strickland & Stevens 2000), for example, although some ULIRG winds appear to require starburst regions extended to $\gtrsim 1 \text{ kpc}$ to launch the cool outflow (Martin 2006). Previous hydrodynamic simulations have shown that extended, multiple energy sources, as well as a single central energy source, forms a bipolar outflow (Fragile et al. 2004). We therefore start with this oversimplified assumption and do not expect the results to differ much from those expected with more extended star forming regions.

In addition, we neglect the effects of UV radiation on molecular hydrogen in the disk. The UV radiation from massive stars may photo-dissociate some of molecular hydrogen outside star-forming cores to atomic hydrogen. However, the assumed turbulent pressure with $c_s = 55 \text{ km s}^{-1}$ is 14 times greater than the increased thermal pressure by photo-dissociation. We thus safely neglect the effects of UV radiation on the disk gas structure.

We define the model with $\Sigma_0 = 10^4 \text{ M}_\odot \text{ pc}^{-2}$ and $L_{\text{mech}} = 10^{43} \text{ erg s}^{-1}$ as our fiducial model (U1/X1). We list the parameters for all the other runs in Table 1.

2.3. Bubble Dynamics

In the molecular disk of a ULIRG with a very small scale height, a bubble with $L_{\text{mech}} \geq 10^{41} \text{ erg s}^{-1}$ quickly blows out of the disk at $t \ll 1 \text{ Myr}$. We can only simulate the evolution of the bubble up to $t \sim 0.3 - 1 \text{ Myr}$ before it leaves our grid, which is rather small because of the cost of high resolution. We argue in § 5 that cooled, swept-up shells, which we identify as Na I absorbing gas, can acquire maximum velocities primarily determined by when they

blow out, accelerate, and fragment. The question remains whether these shell fragments and clumps survive as the hot interior wind streams through them.

Each individual shell fragment after blowout remains unstable to smaller scale R-T instabilities while being further accelerated by the wind, requiring extremely high resolution to fully resolve. Resolution is not as critical for previously published numerical studies on starburst winds that explored feedback parameters. For example, reasonable assumptions about cooling losses indicate that moderate luminosity starbursts do not remove a significant fraction of the galaxy’s gas from the halos (Mac Low & Ferrara 1999), and the mass loss rates would only decrease further with more cooling. A large fraction of the heavy elements do escape from the halos (Mac Low & Ferrara 1999; Fujita et al. 2004), and this result does not depend on resolution below \sim a few tens of parsecs, so long as at least a few R-T modes are excited in the swept-up shells to let the metal-enriched gas escape. Therefore, a major question that must be answered to understand observations of cold gas at high velocity is whether clumps of dense gas survive in the lower density wind (cf. Klein et al. 1994; Marcolini et al. 2005), where they will fragment because of hydrodynamic instabilities, such as R-T (strictly speaking, Richtmyer-Meshkov; see Richtmyer 1960), and Kelvin-Helmholtz.

Weaver et al. (1977) argued that the density in the hot interior of bubbles in uniform gas is dominated by conductive evaporation from the dense shell. However, our model does not explicitly include thermal conduction, or material ablated off of high-density molecular clouds associated with the central starburst. Instead, we add additional mass to our central luminosity source to account for this process, multiplying the mass input rate by a mass-loading factor ξ . The amount of thermally evaporated mass in a bubble expanding into a uniform medium is proportional to $L_{mech}^{27/35} \rho^{-2/35}$. The internal temperature is

$$T_b(t) = (\gamma - 1) \frac{\mu}{k_B} \left[\frac{5}{11} \int_0^t L_{mech}(t') dt' \right] / \left[\int_0^t \xi M_{SN}(t') dt' \right]. \quad (2)$$

where $L_{mech}(t)$ and the mass of supernova ejecta $M_{SN}(t)$ as a function of time are taken from Starburst 99 model, the adiabatic index $\gamma = 5/3$, mean mass per particle $\mu = 14/22 m_H$, and k_B is the Boltzmann factor. We assume that 5/11 of the total mechanical energy goes into the hot, pressurized region bound by the inner and outer shock fronts based on the classic superbubble theory (Castor et al. 1976; Weaver et al. 1977, Mac Low & McCray 1988). We show $T_b(t)$ in Figure 3a.

We can estimate the terminal velocity of the wind driven by such a bubble as

$$v_{wind}(t) = 2 \left[\frac{5}{11} \int_0^t L_{mech}(t') dt' \right] / \left[\int_0^t \xi M_{SN}(t') dt' \right], \quad (3)$$

which we plot in Figure 3b. Since the mechanical luminosity $L_{mech}(t)$ and the mass of supernova ejecta $M_{SN}(t)$ are both linearly proportional to the amount of gas converted to

stars, T_b and v_{wind} are the same for all strengths of starburst with the same mass-loading rate ξ . We take a fiducial ξ value of about 8 corresponding to a mass-loading rate $\dot{M}_{in} = 17(L_{mech}/10^{43}) \text{ M}_{\odot} \text{ yr}^{-1}$, but run test simulations with ξ varying between ~ 1 –15 to explore the effects of mass-loading on the shell kinematics. Comparisons to observations suggest $\xi \approx 10$ (Suchkov et al. 1996 – see M82 comparison; Martin et al. 2002). Throughout this paper, we designate as the wind the hot interior gas freely streaming outwards after blowout of the shell.

3. Numerical Methods

We follow the numerical methods used by Mac Low & Ferrara (1999) and Fujita et al. (2003) to model a starburst in a galactic disk. We briefly summarize our methods below, but refer to the papers above for more details. We compute the evolution of a starburst-driven blastwave as it blows out of the molecular disk of a ULIRG with ZEUS-3D¹, an Eulerian, finite-difference, astrophysical gas dynamics code (Stone & Norman 1992; Clarke 1994), that uses second-order van Leer (1977) advection, and a quadratic artificial viscosity to resolve shock fronts. We use the loop-level parallelized version ZEUS-3D, in its two-dimensional form. Runs were done on Silicon Graphics Origin 2000 machines using eight processors, and typically took ~ 1 –12 days.

We assume azimuthal symmetry around the rotational axis of the galaxy. Our fiducial grids are 1000×500 zones with a resolution of 0.2 pc, comparable to the size of star-forming cloud cores. We also run the same simulations with resolution of 0.1, 0.4, and 0.8 pc to examine the sensitivity of post-shock shell density and thus R-T instability growth to resolution. We use reflecting boundary conditions along the symmetry axis and along the galaxy midplane and outfall boundary conditions on the other two axes.

To drive a constant luminosity wind, we add mass and energy to a source region with a radius of 10 pc (50 zones). Our fiducial mass input rate is $\dot{M}_{in} = 17(L_{mech}/10^{43}) \text{ M}_{\odot} \text{ yr}^{-1}$ which corresponds to a mass-loading factor $\xi \approx 8$. For simulations with different resolutions, we keep the the number of zones covering the spherical edge of the source regions the same by maintaining its radius as a constant number of zones rather than a constant physical size. This is important because aliasing at the edge creates density perturbations that can be amplified by hydrodynamic instabilities, such as the R-T instability in the swept-up shell. We use ratioed grids for lower-resolution runs and we decrease the size of source region to a radius of 5 pc (50 zones) for a higher-resolution run. We directly show the effects of this

¹Available from the Laboratory for Computational Astrophysics, <http://cosmos.ucsd.edu>

initial noise on the development of R-T instability by running a simulation with a resolution of 0.2 pc, but with a source region with a radius of 5 pc (25 zones).

As in MF99, we use a cooling curve by MacDonald & Bailey (1981) for solar metallicity with a temperature floor of either $T_{\text{floor}} = 10^2$ K, the temperature to which the metals can cool the gas, or 10^4 K, the temperature maintained by photoionization heating. The shocked gas in swept-up shells cools efficiently to the temperature floor set in the cooling curve, since our molecular disk is very dense. We show in § 4.2.2 that even our highest resolution runs do not yet fully resolve the dense shells even for $T_{\text{floor}} = 10^4$ K, so the influence of the cooling floor is not evident in our work. We also include an empirical heating function tuned to balance the cooling in the background atmosphere. This is linearly proportional to density, so that it is overwhelmed by cooling in compressed gas which is proportional to the square of the density (Mac Low et al. 1989). This is to prevent the background atmosphere from spontaneously cooling. We use a tracer field (Yabe & Xiao 1993) to turn off radiative cooling in the hot bubble interior, in order to prevent mass numerically diffused off the dense shell from spuriously cooling the interior. The cooling time of the interior is much longer than the dynamical time of our bubble, so interior cooling is physically unimportant to the bubble dynamics (Mac Low & McCray 1988). These adiabatic bubble interiors form energy-driven winds after blowout.

4. Parameter Studies

We now describe the results of parameter studies of both physical and numerical variables. We begin by considering physical variables, including mechanical luminosity, mass-loading of the wind, and disk surface density. We then discuss numerical variables, focusing on how numerical resolution and the cooling cutoff temperature affect shell density and also examining the effect of changing the size of the source region.

4.1. Physical Parameters

4.1.1. Mechanical Luminosities

Our fiducial model (X1) has mechanical luminosity $L_{\text{mech}} = 10^{43}$ erg s⁻¹. This model corresponds to the first 2 Myr of a starburst in which 10^9 M_⊙ of gas turns into stars instantaneously. We compare this to models with lower mechanical luminosities $L_{\text{mech}} = 10^{42}$ and 10^{41} erg s⁻¹ (models X2 and X3 respectively) in the same molecular disk. These mechanical luminosities correspond to instantaneous bursts of 10^8 and 10^7 M_⊙. Figure 4

shows the density distribution of our fiducial model in its right panel. This may be compared to Figure 5, which shows the density distributions of the two models with lower L_{mech} at $t \approx 0.49$ Myr and 0.85 Myr respectively. The swept-up shells fragment due to R-T instability into multiple clumps and shells.

Secondary Kelvin-Helmholtz instabilities ablate the sides of these fragments as the hot gas streams through them. Look at the clumps, for instance, at $(R,Z) \approx (40, 65)$, $(30, 110)$, and $(15-25, 120)$ pc in X1. Note also that the swept-up shells in the horizontal direction are also R-T unstable, because our disk gas is stratified in the radial direction, too, due to its exponential surface density profile.

In fact, the degree of fragmentation is larger in X2 and more so in X3 because $\dot{M}_{in} \propto L_{mech}$ and so the density of interior gas is lower. In particular, most shell fragments in X3 are already falling back to the disk. A mechanical power of 10^{42} erg s $^{-1}$ is just too small in such a dense environment to accelerate the bulk of the shells to the disk’s escape velocity.

4.1.2. Surface Density

The top right panel of Figure 5 shows the density distribution of our model with $M_d = 10^{10} M_\odot$, but with a higher surface density, $\Sigma_0 = 5 \times 10^4 M_\odot \text{ pc}^{-2}$ at $t = 0.22$ Myr (V1). With the same mechanical luminosity, $L_{mech} = 10^{43}$ erg s $^{-1}$, the bubble blows out earlier at $t \approx 0.15$ Myr, because the disk is more stratified with a smaller scale height (see Figure 1). Except the time of blowout, the degree of fragmentation and the shell kinematics are about the same in models with surface densities different by a factor of five.

4.1.3. Mass-Loading

Mass-loading from thermal conduction and molecular clouds determines the density of the bubble interior and wind. Figure 6 shows the density distributions of our fiducial ULIRG model with $T_{floor} = 10^2$ K with mass-loading rates of 1.7, 17, 49, and 120 $M_\odot \text{ yr}^{-1}$ (models U1-A, U1, U1-B, and U1-C). These mass-loading rates correspond to bubble interior temperatures, $T_b = 1.7 \times 10^8$, 2.2×10^7 , 7.5×10^6 , and 3.2×10^6 K and wind terminal velocities expected when all the thermal energy is converted to kinetic energy, $v_{wind} = 2700$, 1000, 600, and 250 km s $^{-1}$ respectively.

Figure 6 shows the bubbles just before they leave the grid, at $t = 0.23$, 0.27, 0.35, and 0.41 Myr respectively. Since the input mechanical luminosity is the same in all these models the bubbles initially grow at about the same rate, driven by the thermal pressure

of the hot interior gas. However, a bubble with a lower mass-loading rate and higher wind terminal velocity expands faster into the halo once the swept-up shells fragment and the hot gas blows out between the fragments. In addition, the blowout occurs earlier and in more places with a lower mass-loading rate because the density of the bubble interior gas is lower. A higher density contrast between the hot interior and the swept-up shells promotes shell fragmentation by R-T instability, the growth of which is proportional to the density contrast. In the least dense model U1-A, all the swept-up shells quickly fragment into fingers and filaments and the dense clumps at their edges are subject to secondary Kelvin-Helmholtz instabilities.

As the hot bubble interior becomes transonic after blowout, it accelerates the shells and shell fragments by ram pressure rather than thermal pressure. This low-density wind thus can accelerate the shells to higher velocity after blowout. We quantitatively study the effects of wind ram pressure in the next section (§ 5.4). The observed X-ray temperature T_X is $\sim 0.67 \text{ keV} = 7.7 \times 10^6 \text{ K}$ in all kinds of starburst galaxies from dwarfs to ULIRGs (Martin 1999; Heckman et al. 2001; Huo et al. 2004; Grimes et al. 2005). This corresponds to $\xi \approx 10$ in equation 3. However, the X-ray emission is proportional to n^2 so it is biased toward high-density regions such as the interface between the hot interior gas and the shells and their fragments. At this interface, conductive evaporation and turbulent ablation raise the density. The recent observations of diffuse hard X-ray emission in starburst galaxies suggest the existence of a very hot ($\log T \gtrsim 7.5$) metal-bearing gas (e.g. Strickland et al. 2004; Strickland & Heckman 2007). Then the bulk of the hot wind may still be very hot $\sim 10^8 \text{ K}$, the temperature which Strickland & Stevens (2000) modeled for M82 with $\xi = 1$.

4.2. Numerical Parameters

4.2.1. Grid Resolution

Figure 7 shows the density distributions of our fiducial model with grid resolution varying from 0.1 to 0.8 pc. We chose $T_{\text{floor}} = 10^4 \text{ K}$ for this resolution study, because shell densities are not too far from what we expect analytically with this high minimum temperature. The growth of R-T instability is significantly enhanced in the highest resolution run, X1-0, and suppressed in the lower resolution runs, X1-2 and X1-4. In particular, all the outermost shells seen in X1 further fragmented by R-T instability in X1-0 with the resolution increased only by a factor of two. The positions of outer shock fronts in the horizontal direction agree very well among the four simulations, since the shells there are not subject to severe hydrodynamic instabilities.

Figure 8 shows the density profiles at the outer shock fronts before any fragmentation occurs for the runs in our standard resolution study. The bubble in our highest resolution run X1-0 grows a little slower in the beginning, because we chose the size of the source region in X1-0 to be half of that in X1 in order not to overproduce noise at the contact discontinuity. We will show below that this noise feeds R-T instability and must be maintained the same in order to study the effects of resolution on shell fragmentation alone. Thus the density profile of X1-0 at $t = 0.06$ Myr is not directly comparable to those of other runs at $t = 0.05$ Myr, but Figure 8 still demonstrates the trend in resolving the peak shell density as a function of resolution.

Figure 8 shows that the shell density is progressively better resolved as the resolution increases. However, the cooling times at the shock front are typically of order 10^2 yr (see § 4.2.2), so a shock with cooling floor equal to the background temperature of 10^4 K may be treated as isothermal. At the time displayed, the Mach number of the outer shock is $\mathcal{M} = 19$. The shell density we expect from an isothermal shock propagating into a background density ρ_{bg} is $\rho_{bg}\mathcal{M}^2 = 6.1 \times 10^{-19}$ g cm $^{-3}$. Figure 8 shows that the shell density ρ_{shell} is still unresolved by a factor of ~ 4 even with our highest grid resolution of 0.1 pc.

The difference we see in the development of R-T instability develops because of two factors. First, the post-shock density of the swept-up shells is not fully resolved. Increasing density contrast drives faster R-T growth. Second, the linear R-T instability grows more quickly at smaller wavelengths, but the nonlinear development moves to increasing larger wavelengths as competition between growing modes becomes important (Youngs 1984). At least 10–25 zones is required to resolve the smallest modes, though (e.g. Mac Low & Zahnle 1994), so grid resolution matters critically for the initial development and transition to nonlinearity. However, we believe that we reached the point where resolution effects are no more important than physics we have not included such as magnetic fields, non-equilibrium cooling, thermal conduction, and photoionization, as well as the assumption of azimuthal symmetry (i.e. fragments are confined in rings).

For example, strong magnetic fields $B \sim 20\mu G$ observed in the Antennae merging galaxy (Chyży & Beck 2004) can potentially inhibit the formation of cold, dense shells or suppress their fragmentation. Our study does show that the degree of R-T fragmentation is important to reproduce the observed wide range of cooled shell fragments. Recall, however, that the shell density in our simulations can be more than an order of magnitude underresolved. Thus the degree of fragmentation will not be significantly overestimated in our simulations unless the magnetic fields are strong enough to reduce the shell density by more than that.

The density ρ_{sh} expected behind an isothermal shock running into a magnetic field with Alfvénic Mach number \mathcal{M}_A and having $1 \ll \mathcal{M}_A \ll \mathcal{M}$ is $\rho_{sh} = \rho_0\sqrt{2}\mathcal{M}_A$ (Draine & McKee

1993). Before the effects of magnetization become important in limiting R-T instability, the ratio between the magnetized and unmagnetized post-shock densities must be of order $2^{1/2}\mathcal{M}_A/\mathcal{M}^2 < 10^{-2}$. With $\rho \sim 10^{-24} \text{ g cm}^{-3}$ and $v_s = 500 - 800 \text{ km s}^{-1}$, the shell density expected with $B \sim 20\mu\text{G}$ becomes three order of magnitude lower than that without B. The effect of magnetic field thus becomes substantial only when a bubble grows to the high-Z, low-density part of the disk, above $Z > 100 \text{ pc}$. However, most of the fragmentation occurs within $Z \sim 100 \text{ pc}$ especially with the highest-resolution run, Thus our results on the wide absorption profiles are robust. If anything, the suppression of fragmentation by magnetic pressure at high latitude will allow the hot wind to keep accelerating the outermost shells. Magnetic pressure might thus even increase the amount of cool gas with high terminal velocity.

We also note that resolving the shell density profile is not important to following the overall dynamical evolution of bubbles driven by the thermal energy of the hot, pressurized regions (Castor et al. 1975; Weaver et al. 1977), but is important to follow the details of shell fragmentation due to R-T instability and the fate of dense fragments and clumps by shocks and following hydrodynamic instabilities. We will show below that the resolution of 0.2 pc is still not sufficient to properly model hydrodynamic instabilities acting on shells and clumps, but is just sufficient for the purpose of demonstrating a wide range of velocities in shell fragments caused by R-T instability.

4.2.2. Cooling Temperature Floor

We show the density distributions of our fiducial model with different cooling curve cut-offs of $T_{\text{floor}} = 10^2 \text{ K}$ (U1) and 10^4 K (X1) at the time of blowout in Figure 4. Figure 4 shows that the temperature floor we choose for our cooling function appears to have a negligible influence on the evolution of bubbles in our models.

However, closer examination reveals that the density of shocked shells is approximately the same in both simulations despite the difference in temperature floor. For example, at $t = 0.05 \text{ Myr}$ before any fragmentation occurs, the shell density in both simulations is $\sim 8 \times 10^{-20} \text{ g cm}^{-3}$ in the vertical direction where the background disk density is $\rho_{bg} = 2 \times 10^{-21} \text{ g cm}^{-3}$. This is because the density peak in the simulations is limited by resolution in these models, not by the strength of cooling. The shock velocity in the vertical direction at $t = 0.05 \text{ Myr}$ is $\sim 230 \text{ km s}^{-1}$, or Mach number $\mathcal{M} = 15$ in 10^4 K background gas. The immediate post-shock temperature is then $T = 7.6 \times 10^5 \text{ K}$. This shocked gas quickly cools to or below 10^4 K because the exponential cooling time (e.g. Mac Low & McCray 1988) is

very short,

$$\tau_{cool} = 3kT/4n_{bg}\Lambda \approx 64 \text{ yr}, \quad (4)$$

with the mean mass per particle $\mu = 14/22 m_H$ for ionized gas, and $\Lambda(T) = 4.1 \times 10^{-23} \text{ erg cm}^3 \text{ s}^{-1}$ from the MacDonald & Bailey (1981) cooling curve.

The shell density expected from an isothermal shock will then be $\rho_{shell} = \rho_{bg}\mathcal{M}^2 \approx 5 \times 10^{-19} \text{ g cm}^{-3}$ with Mach number $\mathcal{M} = 15$ if $T_{floor} = 10^4 \text{ K}$. If $T_{floor} = 10^2 \text{ K}$, the shell density will reach values even greater than the isothermal value. However, since the shell density is far from being resolved even with 0.1 pc resolution in our simulations, the cooling floor has a negligible influence on our models.

4.2.3. Effects of Source Region on Shell Fragmentation

The *top left panel* of Figure 5 shows the density distribution of our fiducial model with $T_{floor} = 10^4 \text{ K}$, but with a source region of a smaller radius of 5 pc or 25 zones (S1). The density structure of S1 looks very similar to that of X1, but the fragmentation by R-T instability is slightly suppressed. This is because a smaller number of cells is covering the edge of the spherical source region in which the density is imperfect. This imperfection creates a perturbation which gets amplified by hydrodynamic instabilities. A much smaller source region will make a bigger difference in the amount of fragmentation. It is important to note that we are anyway probably underestimating the degree of fragmentation since our bubble sweeps up a smooth, one-phase ISM instead of real ISM which density is highly fluctuating from the smooth mean.

5. Comparison to Observations

In this section, we first use the ballistic approximation to justify making a comparison between the observations and our simulations in which the bubbles are evolved only up to $t \ll 1 \text{ Myr}$. Then, we identify gas parcels likely to produce Na I absorption, and simulate observations of this gas along sightlines towards the galactic nucleus. The velocity spread, the mass-weighted velocity, and the maximum velocity are compared for different viewing angles. The velocity gradient across one of these winds is also studied for comparison to longslit spectra. We then compare our models to the observed Na I absorption profiles.

5.1. Ballistic Approximation

We use a limited grid size in order to maintain high resolution, so we simulate the evolution of bubbles only up to the time of blowout. We showed in the previous section that the bubbles blow out very early, at $t \ll 1$ Myr, because of the small scale height of our molecular disk. For comparison, ultraluminous starbursts have ages of up to 50 Myr (Murphy et al. 2001). To extrapolate our computational results to later times, we use the ballistic approximation (Zahnle & Mac Low 1995; Fujita et al. 2004) that after blowout, shell fragments travel on radial ballistic orbits in the gravitational potential of the galaxy, with no further accelerations by gas pressure gradients. Even if the stronger winds expected from supernovas at late times in an instantaneous starburst (see Figure 2) do accelerate the fragments further, the ballistic approximation will still yield a lower limit to their velocities.

This simple approximation was successfully used by Zahnle & Mac Low (1995) to follow the ejecta of a typical Shoemaker-Levy 9 fragment falling back to the Jupiter’s atmosphere, and was found to give results consistent with the observations. Under the ballistic approximation, the equation of motion for a shell fragment at a distance r from the galactic nucleus is

$$v(r) = \{v^2(r_b) + 2[\Phi(r_b) - \Phi(r)]\}^{1/2}, \quad (5)$$

where $\Phi(r)$ is the total halo and disk potential, and $v(r_b) = v_b$ is the shell velocity at blowout at a position of r_b .

In Figure 9, we plot $v(r)$ for several initial velocities starting at a fixed initial position, $r_b = 200$ pc, just above our model disk. By setting $r_b = 200$ pc, we can ignore the disk potential which is negligible above the disk compared to the halo potential. Thus we set $\Phi = \Phi_{halo}$ in equation (5) and solve the equation analytically using equation (1). The upper limit to the radius reached by a shell fragment at time t is given by the linear approximation $r \leq v_b t$, because the shell will only decelerate in the potential. We show actual radii for different initial velocities at $t = 10$ Myr by vertical ticks in the left panel of Figure 9. Although Figure 9 is plotted as a function of radial velocity, we find similar results if total velocity is used instead, because shell fragments are traveling in nearly radial directions. This figure shows that the linear approximation is quite good for $v_b > 100 \text{ km s}^{-1}$, so we use it to follow the cold gas for times of order 10 Myr.

For times $t \gg 100$ Myr, the linear approximation fails and most gas falls back to the center after reaching heights of a few hundred kpc. Only gas with $v_b \gtrsim 1000 \text{ km s}^{-1}$ can completely escape our halo, which has escape velocity $v_{esc} = 800 \text{ km s}^{-1}$ at the virial radius $R_v \sim 350$ kpc. We show below that very little gas actually escapes the halo, with $\lesssim 0.1\%$ of the total shell mass accelerated above $v_b \gtrsim 1000 \text{ km s}^{-1}$ in our fiducial model. Our results

confirm the result from previous simulations of smaller galaxies that the loss of ISM mass is inefficient (e.g. Mac Low & Ferrara 1999; D’Ercole & Brighenti 1999). However, significant mass is circulated over scales of 10 kpc, presenting a significant absorption cross section as suggested by Martin (2006).

5.2. Cool Gas

Only the coolest gas can be observed in Na I absorption. We chose a temperature cut-off of $T < 5 \times 10^4$ K to trace this gas because cooling remains numerically limited even with our highest resolution grid. Gas below this cut-off is so dense that the cooling time (eq. 4) is very short, $\tau_{cool} < 0.01$ Myr, so it is physically expected to reach temperatures where Na I is present. As an example, the least dense shell fragment in Figure 10 has $\rho = 3.0 \times 10^{-24}$ g cm $^{-3}$ and $T = 3.3 \times 10^4$ K. Equation (4) gives an exponential cooling time $\tau_{cool} \approx 0.007$ Myr, using $\Lambda(T) \approx 4.2 \times 10^{-23}$ erg cm 3 s $^{-1}$ from the MacDonald & Bailey (1981) cooling curve.

Figures 10 and 11 show the gas density, temperature, and radial velocity in models X1 and X1-0 along a line of sight through the central continuum source at an angle $\theta = 19^\circ$ from the vertical axis. Notice that our temperature cut-off picks up only the densest and the coolest parts of the shells excluding numerically diffused interfaces between the shells and the hot gas. We now compare the characteristics of this temperature-selected gas to the measured properties of Na I absorption in ultraluminous starbursts.

5.2.1. Cool Gas Column Densities

Figure 7 shows that the lines of sight plotted in Figures 10 and 11 go through multiple distinct shells, adding to a total column density of cool gas $N_H \sim 7 \times 10^{21}$ cm $^{-2}$. The inferred column densities in ultraluminous starbursts are a bit lower, exceeding 10^{21} cm $^{-2}$ in only one out of four ultraluminous starbursts (Martin 2005). Since the model column densities fluctuate by as much as an order of magnitude between neighboring sightlines, we plot the column density distribution as a function of angle in Figure 12. We find that most sightlines with $N_H > 5 \times 10^{22}$ cm $^{-2}$ lie within 30° of the galactic disk where the shells are usually not subject to hydrodynamic instabilities. The typical value is $N_H \sim 10^{22}$ cm $^{-2}$, similar to the largest column density estimated from observations of ultraluminous starbursts (Martin 2005, 2006; Rupke et al. 2002).

5.2.2. Geometric Dilution

The column densities found in our model are measured at a time very early in the lifetime of the wind, when it has not expanded far away from the galaxy. However, these winds will typically be observed at later times, when the wind has expanded further. Geometric dilution will then reduce the column density along any particular line of sight even if the gas simply expands radially outwards on ballistic orbits. For spherical geometry (of any opening angle) and constant velocity flow, the volume-averaged gas density declines with increasing radius. The amount of dilution is therefore determined by the radial advance of the innermost cold gas. At early times, see Figure 7 this innermost cold gas lies at a radius of ~ 100 pc, near the wind termination shock. Assuming the cold gas directly above the starburst region flows upward on a ballistic path, we would expect it to move outward by a factor of roughly 100 in the next 25 Myr, reducing the cold gas column density by the same factor.

5.2.3. Resolution Effects

A second reason we overestimate the cool gas column density is that we do not fully resolve the complete fragmentation of the shells. However, as discussed above in § 4.2.1, the overall kinematics described in § 5.1 should remain similar unless shell fragments are entirely mixed with hot gas and destroyed. To distinguish real physical effects from numerical artifacts, we study the kinematics of the cold gas along a $\theta = 19^\circ$ line of sight in our fiducial simulation X1 and the high-resolution simulation X1-0.

The first two fragments from the center are parts of a filament remaining from the initial fragmentation of the swept-up supershell due to R-T instability at $t \sim 0.1$ Myr. These high-density peaks are traveling with similar velocities $v \sim 400 - 500 \text{ km s}^{-1}$ in both simulations and dominate the column densities of cool gas in the studied sightlines. The outermost shell in X1 keeps sweeping up high-altitude disk gas, while in X1-0 this shell further fragments by R-T instability to the last two fragments in Figure 11. The coherence of the shell in X1 clearly occurs because of the lower resolution in that run. However, the shell in X1 and the outermost fragment of the two in X1-0 travel with similarly high velocity of $\sim 800 - 900 \text{ km s}^{-1}$, though they contribute very little to the total column density.

The hot wind overruns and shocks the first fragment in X1 and the first two fragments in X1-0. As a result, secondary R-T and K-H instabilities act on them, removing gas from the cold cloud and mixing it into the hot wind. In both cases, these clumps of gas are resolved by about ~ 10 cells, demonstrating that this is a minimum size below which fragments tend to survive because the secondary instabilities cannot be resolved. Mac Low & Zahnle (1994)

show that fragments must be resolved by at least 25 zones to resolve the secondary instabilities. Fragments smaller than that remain as artificially massive clouds in our simulations, overpredicting the cool gas column densities.

Klein et al. (1994) suggest that these clumps of gas should be destroyed, via hydrodynamic instabilities, over ~ 10 shock crossing timescales

$$t_{cc} = r_c(v_w - v_c)\sqrt{\frac{\rho_c}{\rho_w}} = (0.04 \text{ Myr}) \left(\frac{r_c}{2 \text{ pc}}\right) \left(\frac{v_w - v_c}{500 \text{ km s}^{-1}}\right) \left(\frac{\rho_c/\rho_w}{100}\right)^{1/2}, \quad (6)$$

where r_c is the radius of the clump, ρ_w and ρ_c are the density, and v_w and v_c are the velocity of the wind and the clump, and the scaling parameters hold for typical 10 zone clumps in our model. In reality, t_{cc} may be substantially longer because the density ratios ρ_c/ρ_w are probably underestimated: shell densities, and thus clump densities, are underresolved, while the wind density may be overestimated by our mass-loading scheme. We need $\rho_c/\rho_w \approx 10^4$ for these clumps to survive for more than ~ 5 Myr, which may just be reachable in a rapidly diverging wind. Moreover, recent numerical studies including thermal conduction suggests that this may stabilize clumps against Kelvin-Helmholtz instabilities, reducing mass loss (Marcolini et al. 2005, Vieser & Hensler 2007). Since we are not able to address the fate of shell fragments further in this study, we assume the bulk of the cool mass remains cool for the duration of starburst to be observed as Na I absorbing gas. Larger, denser clumps are more likely to survive, in reality.

5.3. Velocity Spread

The bottom left panels of Figure 10 and 11 show the distribution of column density of cool gas N_H as a function of its radial velocity v_r at the end of the simulations. So long as the linear version of the ballistic approximation is correct, the velocity spread remains constant. Cool gas is seen over a wide range of velocities $> 450 \text{ km s}^{-1}$ at both resolutions. Shells that fragment earlier have been accelerated less, and so their fragments travel more slowly. We now explore whether absorption from multiple shell fragments can explain the large absorption line widths measured for ultraluminous starbursts by considering the effects of resolution and viewing angle.

Figure 13 shows the distribution of velocity widths Δv seen in cool gas with $T < 5 \times 10^4$ K in runs X1-0, X1, X1-2, and X1-4, with grid size increasing from 0.1 to 0.8 pc, along sightlines spaced by 1° from the vertical axis. We define Δv as the difference between the maximum and the minimum velocities seen in the cool gas along a given sightline—that is, full width at zero. This resolution study demonstrates that the fraction of sightlines with

large velocity spread increases as the resolution improves up to 0.2 pc, but then appears to converge.

Comparison to Figure 7 shows that the largest velocity widths are seen in sightlines intersecting the largest number of fragmented shells. Resolving post-shock densities in the swept-up, cooled, shells better leads to more shell fragmentation, producing the wider range of velocities in the fragments.

Figure 13 also shows that most sightlines in X1 and X1-0 are above the average observed line width $\langle v \rangle = 320 \pm 120 \text{ km s}^{-1}$ (*dashed lines*). Observers measure the average of the sightlines toward continuum sources subtending about an arcsecond, and this corresponds to a length of $1.84 h_{0.7} \text{ kpc}$ at redshift 0.1. Assuming that the observers are likely to view ULIRGs at $t = 5 - 10 \text{ Myr}$ after the onset of starburst, we can suggest all the shell fragments within $\sim 20^\circ - 40^\circ$ at a given sightline in our simulations will contribute to the absorption profiles. Hence, our models suggest that observers will measure a large line width regardless of viewing angle.

To quantify this, we compute the average velocity width of all sightlines in an axisymmetric cone within θ as

$$\overline{\Delta v}(\leq \theta) = \frac{\int_0^\theta \Delta v(\alpha) \sin(\alpha) d\alpha}{\int_0^\theta \sin(\alpha) d\alpha}. \quad (7)$$

The value of $\overline{\Delta v}$ is lowered by sightlines near the disk midplane where the bubbles are not blowing out and sightlines intersecting holes made by blowout with nearly zero Δv . The average velocity widths are clearly smaller for lower resolution runs, however. We find $\overline{\Delta v}(\theta \leq 30^\circ)$ is 220 km s^{-1} for run X1-0, and 210 km s^{-1} for X1, but only 110 km s^{-1} for X1-4.

5.4. Average Velocity

Figure 14 shows the distribution as a function of angle with degree spacing of mass-weighted average velocities of cool gas v_{av} (*solid lines*) for our standard resolution study (runs X1-0 through X1-4). The average shell velocities plotted may be misleading, since shell mass differs significantly at each sightline. Therefore, we also plot a mass-weighted average shell velocity across a 10° arc centered on each sightline $v_{av,10}$. This ought to be the quantity most directly comparable to observations of the average velocity. On sightlines with multiple fragments, the average mass-weighted velocity reflects the velocity of the more massive fragments lagging behind in the hot wind. These fragment off supershells driven by thermal pressure of the bubble interior first, and accelerate little thereafter. The observable

quantity $v_{av,10}$ shows a clear converging trend with resolution. The converged value toward the pole appears to be under 400 km s^{-1} , with correspondingly lower values at other angles, as shown in Figure 14. Figure 14 suggests that cool gas in shells and their fragments will be observed to be traveling with $v_{av,10} \approx 200 - 350 \text{ km s}^{-1}$ at angles to the pole $\theta < 60^\circ$, the angle where blowout occurs in all models.

Figure 15 shows the distributions of v_{av} and $v_{av,10}$ for models X2 and X3 run with decreasing mechanical luminosity at the same resolution as model X1. The mass-weighted average velocities of shells should depend on the mechanical luminosity L_{mech} driving the bubble by thermal pressure. In a spherical bubble, the dependence would be $L_{mech}^{1/5}$. This dependence is qualitatively borne out by the results showing $v_{av,10}$ monotonically dropping for models X2 and X3 with order of magnitude lower mechanical luminosities. Note the high spike in $v_{av,10}$ of X3 around $\sim 15^\circ$ is biased to a small amount of cool mass present in its vicinity.

The mass-weighted average velocities $v_{av,10}$ in X1 and X2 agree with the observed shell velocity, but $v_{av,10}$ in X3 is well below the observed value. In disks as massive as these, starbursts with mechanical luminosity lower than $10^{42} \text{ erg s}^{-1}$ will not produce the outflow velocities observed in ULIRGs, which average $v_{s,obs} = 330 \pm 100 \text{ km s}^{-1}$.

5.5. Terminal Velocity

5.5.1. Resolution

Figure 14 also shows the distribution of terminal velocity of cool gas v_{term} at each sightline. We define the maximum velocity at blowout as the terminal velocity a shell will ever acquire, following the ballistic approximation (§ 5.1). The maximum velocity of shell fragments is very high, $v_{term} > 500 \text{ km s}^{-1}$ at the angle $\theta < 60^\circ$ where blowout occurs in all the runs. This high-velocity cool gas is found in the fragments of the outermost shells in our highest resolution model X1-0. The hot wind continues to accelerate a piece of shell, sweeping up the ambient gas, until it fragments further. As discussed above, shell fragmentation is very sensitive to resolution. Thus it is important to test the convergence of the mass of high-velocity gas.

Figure 16(a) shows the mass distribution of cool gas as a function of velocity in X1-0, X1, and X1-2 at $t = 0.27 \text{ Myr}$. The fraction of cool gas traveling at high velocities is low. For example, the mass travelling with $v \geq 500 \text{ km s}^{-1}$ is less than a few percent of the total shell mass, and the mass travelling faster than the observed terminal velocity of 750 km s^{-1} is $< 0.1\%$.

However, these results are best understood as upper limits. The amounts of cool gas in the high-velocity end are progressively smaller as the resolution increases. Roughly factor of two decreases in the mass of cool gas with velocities above 500 km s^{-1} occur between runs with factor of two improvements in linear resolution. This suggests that we have not yet converged on the actual mass of high-velocity gas, although we have set good upper limits. We think this high-velocity gas is not likely to go away entirely, even if we run a simulation with a higher resolution and with additional physics. However, we can not fully quantify its amount with our simulations.

The convergence properties of the peak velocity for cold gas v_{term} are somewhat better. The highest resolution models show $< 20\%$ variations, suggesting that the general result is reasonably robust. The observed maximum value of 750 km s^{-1} is consistent with the models at angles $\theta < 60^\circ$.

5.5.2. Mass Loading

Figure 17 shows the distributions of v_{av} , $v_{av,10}$, and v_{term} for simulations with different mass-loading rates and so different wind terminal velocities: U1-A, U1, U1-B, and U1-C. Cool gas has higher terminal velocities in bubbles with hotter winds that themselves have higher velocities. The hottest wind, in model U1-A, has $v_{wind} = 2700 \text{ km s}^{-1}$, while the coldest wind, in U1-C, has $v_{wind} = 250 \text{ km s}^{-1}$. This correlation illustrates that the maximum velocity which a shell (fragment) can be accelerated to is v_{wind} . Figure 16(b) shows the mass distribution of cool gas as a function of velocity for the four runs at the time of blowout. The cool gas with high v_{term} carries only a small amount of mass (see § 5.5.1). For example, the fraction of cool gas with $v > 500 \text{ km s}^{-1}$ is $\lesssim 2\%$ of the total shell mass, and the fraction with $v > 750 \text{ km s}^{-1}$ is $\lesssim 0.5\%$. The bulk of swept-up and cooled gas is driven to $v \sim 400 \text{ km s}^{-1}$ by thermal pressure of hot sonic gas, but a small fraction of it seems to be accelerated to higher velocity by the ram pressure of the same hot gas as it accelerates to supersonic velocities during blowout.

5.5.3. Mechanical Luminosity

The terminal wind velocity (equation 3) in our models X2 and X3 with lower L_{mech} is the same as that of our fiducial model X1, because the ejected mass $M_{SN} \propto L_{mech}$, and we keep the mass-loading factor ξ constant. In all three models $v_{wind} \approx 1000 \text{ km s}^{-1}$.

Figure 15 shows that the terminal velocities of cool gas are not as high as the observed

average terminal velocity, $v_{t,obs} = 750 \text{ km s}^{-1}$ at most sightlines if $L_{mech} \leq 10^{42} \text{ erg s}^{-1}$. It is much harder for the wind ram pressure to accelerate the outermost shells and their fragments to very high velocity, $> 500 \text{ km s}^{-1}$ if their starting velocity at blowout $v_b \lesssim 200 \text{ km s}^{-1}$.

5.5.4. Summary

In summary, the terminal velocity of cool gas is determined by the combination of total mechanical power L_{mech} and wind terminal velocity v_{wind} (determined by the mass-loading rate ξ in our model). Bubble thermal pressure accelerates the bulk of shells to their final velocity before blowout and ram pressure of the hot transonic wind after blowout accelerates a small fraction of the cool gas to much higher velocities. Faster, less mass-loaded winds accelerate cool gas to higher velocities. Our wind is an energy-driven wind, not a momentum-driven wind (Murray et al. 2005). The thermal energy of the hot wind is gradually turning into its kinetic energy by blowout (recall radiative cooling is turned off inside the wind: see § 3). Our model accounts for the observed 750 km s^{-1} terminal velocity of Na I absorbing gas without invoking any additional physics such as radiation pressure.

5.6. Absorption Profiles

To directly compare to observed profiles, we generate Na I $\lambda 5890$ absorption line profiles along sightlines through our simulations, as well as generalizing this procedure to fully model the observed doublet Na I $\lambda, \lambda 5890, 5896$. To generate the profiles, we begin with the line intensity

$$I_\nu = I_\nu(0) \exp^{-\tau_\nu} = I_\nu(0) \sum_{i=1}^N \exp^{-\tau_i} \quad (8)$$

where the optical depth through cell i at frequency ν is τ_i , the sightline intersects N cells, and the background continuum is $I_\nu(0)$. We normalize the continuum by setting $I_\nu(0) = 1$ and compute the profile as a function of the macroscopic velocity of Na I absorbing gas, v . We compute I_ν in the simulations by setting $v = c(\nu - \nu_0)/\nu_0$, and computing the optical depth contributed by each cell in each of 1000 velocity bins. The optical depth in each cell

$$\tau_i(v) = N_{NaI} s \lambda_{NaI} P(\Delta v), \quad (9)$$

(Spitzer 1978) where $N_{NaI, i}$ is the column density of Na I in a cell i , and the absorption cross section s_ν integrated over frequency ν for $h\nu \gg kT$ is $s \approx 2.654 \times 10^{-2} f_{5890}$ with the

oscillator strength $f_{5890} = 0.6$. The Maxwellian velocity distribution function, $P(\Delta v)$, is

$$P(\Delta v) = \frac{1}{\sqrt{\pi}b} \exp -(\Delta v^2/b^2), \quad (10)$$

with $\Delta v = v - v_i$ and $b = \sqrt{2k_B T_i / \mu m_H}$ for thermal broadening. Our simulations do not track chemical abundances, ionization state, or dust depletion, so we do not directly predict the Na I column. For the purpose of illustration, we compute the total Na I column from the total H I gas column using the conversion used by Martin (2005) to estimate $N_{\text{H I}}$ from their $N_{\text{Na I}}$ measurements, $N_{\text{Na I}} = 1.122 \times 10^{-6} N_{\text{H I}}$.

We generated Na I 5890 line profiles along lines of sight through models X1 and X1-0 to show the effect of numerical resolution on the line profiles in Figure 18. Each sightline is described by its inclination from the polar axis of the simulation. The profile shapes reflect the different structure in these simulations. We can for example compare the absorption profiles in the middle left panel in Figure 18 with the density and velocity distributions of shells in Figures 10 and 11. The sightlines at $\theta = 19^\circ$ intersect three and four shell fragments in X1 and X1-0 respectively. Each of these fragments generates a $\Delta v \gtrsim 50 - 100 \text{ km s}^{-1}$ absorption line. A few of these lines are optically thick with the line profile becoming completely black at the line center. As the wind expands, column densities will drop linearly with radius due to geometric dilution. The complex of lines is spread out over $\sim 400 \text{ km s}^{-1}$.

Figure 18 shows that the line profiles from the high and low resolution models present very similar structure for the most part. One minor exception is the minimum velocity. From 10 deg to 20 deg, the line profiles show a sharp cut-off at a velocity $\sim 500 \text{ km s}^{-1}$ in X1, but $\sim 3 - 40 \text{ km s}^{-1}$ in X1-0. This cut-off reflects the velocity of the first R-T fragments that form from the accelerating swept-up shells, which is lower in the high-resolution simulation. The overall lineshape does appear reasonably well converged.

Observers see the average over parallel sightlines subtending a few kiloparsecs of the disk, and must contend with the doublet nature of the Na I line, which has components at 5890 Å and 5896 Å, with almost equal oscillator strength in the optically thin limit. To compare to the actual observed profiles, which have finite optical depths, we generate the Na I 5890/5896 doublet in the frame of Na I 5890 by assuming $f_{5896} = f_{5890}/1.3$, typical of the observed lines in ULIRGs.

We present average line profiles of the doublet over a 20 deg wide set of radial sightlines spaced at degree intervals. Although this is not exactly what is measured, it is comparable because these rays will subtend about 1-2 kpc of the shell when the bubble is $\sim 10 \text{ Myr}$ old, so they intersect the same region of the shell, albeit at slightly different angles. We are actually doing the analysis at an earlier time, when the bubble is a factor of 100 smaller, and

correspondingly higher column density, though, so we also must apply a geometric dilution factor to the column densities.

Figure 19 compares our simulated doublet line profiles, with and without geometric dilution by a factor of 100, to five typical ULIRG spectra from Martin (2005). The widths of the absorption profiles are very similar between our model at $\theta \leq 50^\circ$ where blowout occurs and the observations. The undiluted absorption in our model much exceeds that observed. Our model overpredicts the cool gas column for two reasons (see §5.2). First, because we analyzed the models at a very early time in the starburst. At later times, the spherical expansion of the wind and the cold gas embedded within it dilutes their column densities. Second, the fragmentation of the shell is incompletely resolved, so some material remains cool that in reality would have been mixed into the hot wind. We account for the first factor by directly reducing the column densities, producing the diluted profiles shown in the Figure, which reproduces the observed intensities well.

The ULIRG spectra show absorption beginning from the systemic velocity, and extending to high velocities. Although this zero velocity absorption is absent in Figure 18, it is seen in the simulated doublet profiles shown in Figure 19, as it comes primarily from contributions from the $\lambda 5896$ line of the doublet blueshifted into zero velocity of the $\lambda 5890$ line. (Note our model does not include the contribution from stellar absorption).

5.6.1. Long Slit Observations

Absorption-line observations with long slits have recently been made across ULIRGs. These spectra show the cool outflow is quite extended spatially and sometimes presents a significant velocity gradient (Martin 2006). Our 2D simulations do not include the rotation of the galactic disk, so the wind is launched without any net angular momentum. We examined whether, in the absence of rotation, the position affected the velocity much. Figure 20 shows terminal and mass-weighted average velocity along slits oriented at 30° from the major and minor axes of the disk, using parallel lines of sight through a 3D rotation of the 2D simulation. The absorption properties along the major axis of the galaxy will be symmetric about its center. An asymmetric velocity gradient is produced along the minor axis because one side of the outflow cone is directed more along the sightline. Substantial variations in velocity width and average velocity are seen at ~ 40 pc and ± 30 pc. These occur where sightlines intersect massive, slow-moving shells at $\theta > 45^\circ$ (see Figure 14) as well as light, fast-moving blowout fragments at $\theta < 45^\circ$. On the other hand, very high terminal velocities are seen on most sightlines since they intersect the fast blowout components.

These realistic sightlines encounter both fast-moving and slow-moving gas at various latitudes, unlike the radial sightlines that we studied in previous sections. Our simulations viewed along non-radial sightlines naturally account for a wide velocity range of cool gas starting at $v \approx 0$ and a high terminal velocity.

5.7. Line Widths of Na I Absorbing and H α Emitting Gas

Finally, we crudely try to separate low-ionization, Na I absorbing gas and ionized H α emitting gas in the cooled shell fragments in our simulations. Our aim is to compare the line widths of both components. Heckman et al. (2002) observed no correlation between the absorption and emission line widths for these lines, and drew the conclusion that only one of the lines could originate in the swept-up shells.

To model the H α emission, we need to assume an ionizing photon luminosity Q and the density distribution at a time the galaxy is likely to be observed. Figure 2 shows the ionizing photon luminosities as a function of time for three starburst cases that we consider. Since the propagation of ionization fronts critically depends on both the densities and the positions of shells, we can not extrapolate the density distribution at blowout to $t \approx 10$ Myr using the ballistic approximation. We can, however, still vary the strength of photon luminosity over a few orders of magnitude to examine the effect of attenuating the photon flux by $1/r^2$ on our existing simulations. For example, a shell will experience about three orders of magnitude less photons per unit area after it travels with 500 km s^{-1} for 10 Myr from $r_b = 200 \text{ pc}$. For our purpose of demonstrating the lack of correlation between the line width of Na I absorbing and H α emitting gas, this crude method is sufficient.

To solve for the transfer of ionizing radiation across our grids, we use the photon-conserving radiative transfer code developed by Abel, Norman, & Madau (1999) in the same manner as it was used in Fujita et al. (2003). It computes the propagation of ionization fronts around a point source; in our study this is a central starburst source. This code is a post-processing step that operates on a given density distribution at a given time step in our simulation. However, the ionization fronts propagate sufficiently rapidly to adjust almost instantaneously to a changing density distribution.

Figure 21 shows the column density as a function of velocity for Na I absorbing gas (*diamonds*) and H α emitting gas (*triangles*) in U1 run at $\theta = 13^\circ$ with $Q = 10^{53}, 10^{54}, 1.9 \times 10^{54}$, and $10^{55} \text{ photons s}^{-1}$. With $Q \leq 10^{54} \text{ photons s}^{-1}$, the line widths are very small for H α emitting gas, $\Delta v_{H\alpha} < 100 \text{ km s}^{-1}$, and large for Na I absorbing gas, $\Delta v_{NaI} = 480 \text{ km s}^{-1}$. The densest shell at $r = 110 \text{ pc}$ traps the photons rather effectively. As Q is increased, that

first shell is ionized, but the second shell then traps the photons. The *bottom left* panel shows that the Na I line width is now very small, $\Delta v_{NaI} = 38 \text{ km s}^{-1}$, while $\Delta v_{H\alpha} = 330 \text{ km s}^{-1}$. With $Q \gtrsim 2 \times 10^{54}$, all the shells are ionized. In reality, the transition from large Δv_{NaI} to $\Delta v_{NaI} \approx 0$ should not be this abrupt because many combinations of fragments and clumps are possible within the observers' $10^\circ \times 10^\circ$ field of view. As we note, we are far from presenting realistic distributions of Na I absorbing and H α emitting gas. However, Figure 21 still demonstrates that the line widths of Na I absorbing and H α emitting gas can easily be uncorrelated although they both originate in the swept-up shells.

6. Caveats and Summary

6.1. Caveats

The biggest approximation of our study is that we analyze the kinematics of shell fragments at $t \ll 1 \text{ Myr}$ in our small grids and extrapolate the results by ballistic approximation for comparison with the observations at $t \gg 1 \text{ Myr}$. These dense clumps may further fragment and ultimately be destroyed by R-T and Kelvin-Helmholtz instability as the high-velocity flow of gas from within the bubble streams through them. As the grid resolution of our models increases to 0.1 pc , we begin to resolve the details of hydrodynamic instabilities, though not completely. We thus might have overestimated the contribution from dense shell fragments lagging behind in the hot gas for Na I absorption profiles.

Continuing to evolve our bubbles in bigger grids with the same resolution will not improve our results, because our analysis is limited by numerical resolution as well as the lack of other physics such as magnetic fields, thermal conduction and photoionization. In order to assess how much cold gas remains at later times, we need to resolve the shocks and hydrodynamic instabilities acting on shells and fragments as the wind streams through them. Doing this in a large-scale simulation will be a challenge even using AMR on modern machines.

In addition, it is an oversimplification to assume a single starburst at the disk center for modeling a galactic outflow. In realistic galaxies, we expect multiple star clusters to be scattered around the disks (e.g. Vacca 1996; Martin 1998). A more complicated structure of cool shells and their fragments is expected with a realistic distribution of star formation, which supports our result of wide velocity range in Na I absorbing gas. However, if most supernova energy is dissipated as each supernova or bubble must interact with the dense molecular disk in which cooling is efficient, it will be hard to observe a high terminal velocity in the swept-up shells. For example, the metal ejection and energy transport efficiencies

could vary with spatial distributions of supernovae in dwarf starburst galaxies (Fragile et al. 2004). On the other hand, the bubble overlap may be very efficient in the dense centers of ULIRGs where most of the gas is Jeans unstable. The next obvious step is to study the effects of realistic star formation on the shell kinematics in three dimensional, AMR simulations.

We also note the development of the R-T instability in our model is limited not only by the resolution, but also by the assumption of azimuthal symmetry. Mac Low et al. (1989) pointed out that the typical spike and bubble structure of the R-T instability is limited to rings in an axisymmetric blowout. The detailed structure of the fragments will be different in three dimensions, but finer fragments will only widen their velocity range, and thus are not likely to change our results substantially.

We neglected magnetic fields in this study, but we showed that the effects of magnetic fields are negligible in our simulations (§ 4.2.1, as their main effect is to reduce the peak shell density, and thus the fragmentation, and they don’t act to do so before fragmentation is essentially complete.

6.2. Summary

We study the origin and the kinematics of cool gas that produces Na I absorption lines in galactic winds, using hydrodynamic simulations of the blowout of starburst-driven superbubbles from the molecular disk of ULIRGs. The bubbles sweep up the dense disk gas, which quickly cools to form dense, thin shells. The cooled shells fragment by R-T instability as they accelerate in the stratified atmosphere of the disk. This blowout occurs very early in our models, at $t \ll 1$ Myr in models with $L_{mech} \geq 10^{41}$ erg s⁻¹. The dense fragments left by the R-T instability lag behind the low-density, high-velocity wind. These fragments carry most of the mass that is swept up by the bubbles, and should have the highest column of Na I. The results of our numerical convergence study suggest that superbubble blowout, combined with subsequent geometrical dilution, can reproduce not just qualitative but quantitative properties of the observed lines.

As a result of R-T fragmentation, multiple shell fragments and clumps travel at different velocities. A sightline going through them reproduces the observed broad line width of the Na I absorption profiles: $\langle v \rangle = 320 \pm 120$ km s⁻¹. This result does not appear to depend strongly on physical parameters such as mass-loading rate, mechanical luminosity, or surface density. However, this result requires sufficient numerical resolution to follow secondary fragmentation of the shell, so that any line of sight runs over multiple cold gas fragments.

We find that a resolution of at least ~ 0.2 pc is required to produce this effect, if mass-loading rates remain moderate $\xi \lesssim 10$. The suggestion by Heckman et al. (2002) that swept-up shells will not show a wide range in velocity is based on a hydrodynamic simulation of M82 with a resolution of 4.9 pc (Strickland & Stevens 2000), more than an order of magnitude worse.

The mass-weighted average velocity of cool gas in galactic outflows is found to be $\sim 400\text{--}500$ km s $^{-1}$ among all the models with $L_{\text{mech}} = 10^{43}$ erg s $^{-1}$, but $\lesssim 200$ km s $^{-1}$ in models with $L_{\text{mech}} = 10^{42}$ and 10^{41} erg s $^{-1}$. The bulk of shells and their fragments are accelerated by the thermal pressure of the bubble interior gas, which is proportional to L_{mech} . No other parameters influence the results. The mass-weighted average velocities in our high-resolution simulation with $L_{\text{mech}} = 10^{42\text{--}43}$ erg s $^{-1}$ agree with the observed value $v_{s,obs} = 330 \pm 100$ km s $^{-1}$. A mechanical luminosity of $L_{\text{mech}} = 10^{43}$ erg s $^{-1}$ corresponds to an instantaneous burst of $M_* = 10^9$ M $_{\odot}$ or a continuous SFR = 500 M $_{\odot}$ yr $^{-1}$ at $t < 1$ Myr after the onset of starburst.

As the swept-up shells fragment by R-T instability, the bubble interior gas blows out and becomes a low-density supersonic wind, as its thermal energy is converted to kinetic energy by expansion. The ram pressure of this wind continues to accelerate entrained cold fragments, and to sweep up high-altitude disk gas, producing small amounts of cold gas with velocities approaching the terminal velocity of the wind. The correlation between wind terminal velocities and terminal velocities of cool gas in simulations with different mass-loading rates supports this picture. If the wind velocity reaches $v_{\text{wind}} \gtrsim 1000$ km s $^{-1}$, a significant fraction of sightlines through a simulation encounters a terminal velocity close to or greater than the observed average terminal velocity of Na I absorption profiles $v_{t,obs} = 750$ km s $^{-1}$. The mass of cool gas with such high velocity is less than a few percent of that of the total cool gas, however. These outermost shells and fragments with high velocity do fragment further in our highest-resolution simulation, but their fragments are traveling with similarly high velocity. Although the mass in the high-velocity tail decreased as the resolution is increased, we believe it is not likely to go away entirely in a higher-resolution simulation.

The clumps and fragments seen in the simulations may be observed as Na I absorbing gas or H α emitting gas, depending on the amount of ionizing photons produced from the central starburst source. To study this, we used a ray-tracing method to model the location of the ionization front in our models as a function of time, and so to trace the gas emitting in H α . By varying the photon luminosity, we showed that the velocity range of the ionized and neutral components do not show any correlation with each other. Thus the lack of correlation in the observed line widths of Na I absorbing gas and H α emitting gas does not rule out the swept-up shells as the origin of both components.

The hot wind in our model is purely energy-driven. By construction the interior bubble can never become momentum-driven because radiative cooling is turned off in the bubble interior. Future work must consider whether this mechanism will reproduce the observational results invoked by Murray et al. (2005) in support of momentum-driven outflows being the dominant physics in major starburst galaxies.

We thank M. L. Norman and the Laboratory for Computational Astrophysics for use of ZEUS-3D, R. F. Coker, G. Gisler, R. M. Hueckstaedt, and C. Scovel for the help with getting started with SAGE, and M. K. R. Joung for useful discussions. Computations were performed on the SGI Origin 2000 of the Rose Center for Earth and Space and the QSC machine of Los Alamos National Laboratory (LANL). AF was supported by a cooperative agreement between UCSB and LANL. CLM thanks the Alfred P. Sloan Foundation and the David and Lucile Packard Foundation for support for this work. M-MML was partly supported by NSF grants AST99-85392 and AST03-07854, and by stipends from the Max-Planck-Gesellschaft and the DAAD.

A. Appendix: Blowout in a Dwarf Galaxy with ZEUS and SAGE

A major issue in our simulations is whether we sufficiently resolve the unstable shell during blowout. To further examine this question, in this Appendix we describe a comparison between models of blowout from a dwarf galaxy similar to that described by Fujita et al. (2003) run with ZEUS-3D, and single-grid and AMR versions of SAGE.

SAGE is an AMR hydrodynamic code developed at LANL/SAIC. It is second order accurate using a piecewise linear Godunov scheme (Kerbyson et al. 2001).

The dwarf galaxy has a nominal redshift $z = 8$, and disk mass $M_d = 10^8 M_\odot$. We choose the midplane density of this galactic disk so that it has an exponential surface density profile. We set up the gas in hydrostatic equilibrium with a background dark matter halo potential, with an effective turbulent velocity of 10 km s^{-1} . Mass and energy are injected at the center of the disk, corresponding to a mechanical energy of starburst, $10^{40} \text{ erg s}^{-1}$, with a mass-loading rate of $0.1 M_\odot \text{ yr}^{-1}$. See the details of disk and halo parameters in Fujita et al. (2003).

In SAGE, the cooling is solved with an explicit method that subcycles the cooling source terms, based on a radiative cooling routine that solves for non-equilibrium chemistry (Abel et al. 1997). The timesteps for each subcycle are determined as $\epsilon e / \dot{e}$ where e is internal energy density and $\epsilon = 0.1$. In ZEUS-3D, on the other hand, we assume that the cooling rate is a function of temperature only, using calculations of equilibrium ionization cooling rates by Sutherland & Dopita (1993) with a cut-off at $T < 10^4 \text{ K}$, and ignore inverse Compton cooling for simplicity. The cooling curve is implemented in the energy equation with a semi-implicit method, using a Newton-Raphson root finder.

In order to avoid overcooling in the bubble interior (see §4), we advect two materials independently in SAGE; 1) disk and halo gas and 2) hot, metal-enriched gas injected at the starburst site, and turn off cooling in the latter. SAGE computes hydrodynamics of a multi-material flow, assuming all materials in a cell have the same pressure. The time required to process mixed cells is linearly dependent on the number of materials. In ZEUS-3D we use the tracer field (Yabe & Xiao 1993) to suppress interior cooling.

We ran simulations with and without radiative cooling, and with and without AMR. Table 2 shows the parameters for our computations. With SAGE we use both uniform and AMR grids having a maximum effective resolution of 0.0693 pc . With ZEUS, we use a ratioed grid having the same central resolution as the lowest resolution SAGE runs, and decreasing resolution outside the innermost $0.1 \times 0.2 \text{ kpc}^2$.

SAGE was run on the QSC cluster at LANL using 12 Alpha processors for the UN,

UC, AN, and AC runs, 24 processors for the BC run, and 48 processors for the CC run, while ZEUS-3D was run on a SGI Origin 2000 using 8 processors. SAGE’s performance is linear up to at least a few hundred processors (Kerbyson et al. 2001), while the loop-level parallelized performance of ZEUS-3D levels off after 8 processors (a massively parallel, domain-decomposed version, ZEUS-MP, has linear performance to over 512 processors). The number of active cells used for the AMR simulations with 5 and 6 levels of refinement is less than the number of cells used for the ZEUS-3D simulations. The CPU time per cycle is much smaller with SAGE compared to that with ZEUS-3D, if cooling is included. ZEUS-3D spends the most time searching for convergence around the cut-off temperature of the cooling curve, since radiative cooling in our dense, high-redshift disk is very efficient.

Figure 22 shows the density distributions of our models at the times when the bubbles blow out of the disks. This time was chosen so that the positions of outer shock fronts in the horizontal direction agree. Figure 22 shows qualitative agreement between the results with SAGE and ZEUS. In our no-cooling runs, the positions of outer shock fronts agree within $\sim 2\%$. Those of inner shock fronts agree within $\sim 5\%$ if SAGE is run in the uniform grid and $\sim 10\%$ if SAGE is run with AMR, because we chose an AMR refinement criterion that did not act in that region, while the uniform grid had the resolution of the highest AMR refinement level.

The linear piecewise advection method of SAGE seems more diffusive than the Van Leer method of ZEUS. However, we show in Figure 22 that the SAGE/AMR run begins resolving fine structures caused by R-T instability as well as ZEUS-3D run when one more level of refinement is added, doubling the maximum effective resolution. Even in this case, the SAGE/AMR run still uses a smaller number of total and active cells than the ZEUS-3D run. We can save noticeable computational time with SAGE/AMR as we tackle a problem with more than a few million cells. This advantage will be bigger with three-dimensional models.

REFERENCES

- de Avillez, M. A., & Breitschwerdt, D. 2004, *A&A*, 425, 899
- Blitz, L., & Roslowky, E. 2006, *ApJ*, 650, 833
- Castor, J., McCray, R., & Weaver, R. 1975, *ApJ*, 200, L107
- Chyży, K. T., & Beck, R. 2004, *A&A*, 417, 541
- Clarke, D. A. 1994, NCSA Technical Report.
- D’Ercole, A. & Brighenti, F. 1999, *MNRAS*, 309, 941
- Draine, B. T., & McKee, C. F. 1993, *ARA&A*, 31, 373
- Fragile, P. C., Murray, S. D., & Lin, D. N. C. 2004, *ApJ*, 617, 1077
- Fujita, A., Mac Low, M.-M., Ferrara, A., & Meiksin, A. 2004, *ApJ*, 613, 159
- Fujita, A., Martin, C. L., Mac Low, M.-M., & Abel, T. 2003, *ApJ*, 599, 50 (615, 1082 Erratum)
- Glover, S. C. O. G., & Mac Low, M.-M. 2007, *ApJ*, 659, 1317
- Grimes, J. P., Heckman, T. M., Strickland, D. K., & Ptak, A. 2005, 628 187
- Heckman, T. M., Sembach, K. R., Meurer, G. R., Leitherer, C., Calzetti, D., & Martin, C. L. 2001, *ApJ*, 558, 81
- Heckman, T. M., Lehnert, M. D., Strickland, D. K., & Armus, L. 2000, *ApJS*, 129, 493
- Huo, A. Y., Xia, X. Y., Xue, S. J., Mao, S., & Deng, Z. G. 2004, *ApJ*, 611, 208
- Jimenez, R., Verde, L., & Oh, S. P. 2003, *MNRAS*, 339, 243
- Kompaneets, A. S. 1960, *Soviet Phys. Dokl.*, 5, 46
- Leitherer, C., Schaerer, D., Goldader, J. D., Delgado, R. M. G., Robert, C., Kune, D. F., de Mello, D. F., Devost, D., & Heckman, T. M. 1999, *ApJS*, 123, 3
- MacDonald, J. & Bailey, M. E. 1981, *MNRAS*, 197, 995
- Mac Low, M.-M., McCray, R., & Norman, M. L. 1989, *ApJ*, 337, 141
- Mac Low, M.-M. & McCray, R. 1988 *ApJ*, 324, 76

- Mac Low, M.-M. & Ferrara, A. 1999, *ApJ*, 513, 142
- Mac Low, M.-M., & Zahnle, K. *ApJ*, 434, L33
- Marcolini, A. Strickland, D. K., D’Ercole, A., Heckman, T. M., & Hoopes, C. G. 2005, *MNRAS*, 362, 626
- Marconi, A., Risaliti, G., Gilli, R., Hunt, L. K., Maiolino, R., & Salvati, M. 2004, *MNRAS*, 351, 169
- Martin, C. L. 1998, *ApJ* 506, 222
- Martin, C. L. 1999, *ApJ*, 513, 156
- Martin, C. L. 2005, *ApJ*, 621, 227
- Martin, C. L. 2006, *ApJ*, 647, 222
- Martin, C. L., Kobulnicky, H. A., & Heckman, T. M. 2002, *ApJ*, 547, 663
- Mo, H. J., Mao, S., & White, S. D. M. 1998, *MNRAS*, 295, 319
- Murphy, T. W. J., Soifer, B. T., Matthews, K., & Armus, L. 2001, *ApJ*, 559, 201
- Navarro, J. F., Frenk, C. S., & White, S. D. M. 1997, *ApJ*, 490, 493
- Rupke, D. et al. 2002, *ApJ*, 570, 588
- Rupke, D. et al. 2005, *ApJS*, 160, 115
- Richtmyer, R. D. 1960, *Comm. Pure Appl. Math*, 13, 297
- Salpeter, E. E. 1955, *ApJ*, 121, 161
- Sanders, D. B., Scoville, N. Z., Sargent, A. I., & Soifer, B. T. 1988, *ApJ*, 324, L55
- Schwartz, C. M., & Martin, C. L. 2004, *ApJ*, 610, 201
- Silich, S, A. & Tenorio-Tagle, G. 1998, *MNRAS*, 299, 249
- Silich, S, A. & Tenorio-Tagle, G. 2001, *ApJ*, 552, 91
- Solomon, P. M., Downes, D., Radford, S. J. E., & Barrett, J. W. 1997, *ApJ*, 478, 144
- Scoville, N. Z., Yun, M. S., & Bryant, P. M. 1997, *ApJ*, 484, 702
- Stone, J. M. & Norman, M. L. 1992, *ApJS*, 80, 753

- Strickland, D. K., & Heckman, T. M. 2007, *ApJ*, 658, 258
- Strickland, D. K., Heckman, T. M., Colbert, E. J. M., Hoopes, C. G., Charles, G., & Weaver, K. A. 2004, *ApJS*, 151, 193
- Strickland, D. K. & Stevens, I. R. 2000, *MNRAS*, 314, 511
- Suchkov, A. A., Berman, V. G., Heckman, T. M., & Balsara, D. S. 1996, *ApJ*, 463, 528
- Tenorio-Tagle, G., & Bodenheimer, P. 1988, *ARA&A*, 26, 145
- Tomisaka, K., & Ikeuchi, S. 1986, *PASJ*, 38, 697
- Tomisaka, K., & Ikeuchi, S. 1988, *ApJ*, 330, 695
- van Leer, B. 1977, *J. Comput. Phys.*, 23, 276
- Vieser, W., & Hensler, G. 2007, *A&A*, 472, 141
- Weaver, R., McCray, R., Castor, J., Shapiro, P., & Moore, R. 1977, *ApJ*, 218, 377
- Yabe, T., & Xiao, F. 1993, *J. Phys.Soc. Japan*, 62, 2537
- Youngs, D. L. 1984, *Physica D*, 12, 32
- Zahnle, K. & Mac Low M.-M. 1995, *JGR/E*, 100, 16885

Table 1: Parameters for Starburst Models

Model ^a	$\log_{10} \Sigma_0^b$ ($M_\odot \text{ pc}^{-2}$)	$\log_{10} L_{mech}^c$ (erg s^{-1})	\dot{M}_{in}^d ($M_\odot \text{ yr}^{-1}$)	R_{SN}^e (pc)	T_{floor}^f (K)	resolution (pc)
X1	4	43	17	50	10^4	0.2
X1-0	4	43	17	25 ^g	10^4	0.1
X1-2	4	43	17	50	10^4	0.4 ^h
X1-4	4	43	17	50	10^4	0.8 ^h
U1	4	43	17	50	10^2	0.2
U1-A	4	43	1.7	50	10^2	0.2
U1-B	4	43	49	50	10^2	0.2
U1-C	4	43	120	50	10^2	0.2
X2	4	42	17	50	10^2	0.2
X3	4	41	17	50	10^2	0.2
S1	4	43	17	25	10^2	0.2
V1	4.7	43	17	50	10^2	0.2

^aAll models run with ZEUS

^bCentral surface density

^cMechanical luminosity

^dMass loading rate

^eSize of source region where supernova energy is injected

^fThe minimum temperature floor for cooling

^gThe level of noise on the surface of the source region is kept same with that of our standard model, X1 by setting the number of cells covering the source region the same.

^hRatioed grids are used (the resolution is 0.2pc within the source regions)

Table 2: Parameters for Dwarf Galaxy Models

model	code	initial grid	res ¹ (pc)	cool	AMR ²	cycle	cells ³ active (total)	cpu ⁴ per cycle	procs ⁵
UN	SAGE	800×1120	0.277	OFF	OFF	7244	896	4.0	12
UC	SAGE	800×1120	0.277	ON	OFF	10877	896	4.9	12
AN	SAGE	50×70	0.277	OFF	5	7469	111 (146)	0.86	12
AC	SAGE	50×70	0.277	ON	5	10790	103 (136)	0.84	12
BC	SAGE	50×70	0.139	ON	6	22568	240 (319)	1.5	24
CC	SAGE	50×70	0.0693	ON	7	54000	503 (698)	2.3	48
RN	ZEUS	400×878^6	0.277	OFF	OFF	6035	351.2	70.51	8
RC	ZEUS	400×878^6	0.277	ON	OFF	9036	351.2	3.7	8

Note. — We give the number of cycles, the average numbers of active (with AMR) and total cells, and the average cpu time spent per cycle that are used to run the simulations until the bubbles blow out of the disk.

¹The highest resolution employed in the simulations.

²The level of refinement used in AMR: if OFF, uniform or ratioed grids are used.

³Average numbers of active and total cells used per cycle, in thousands.

⁴The amount of cpu time spent per cycle.

⁵Number of processors used for computation.

⁶Ratioed grids are used.

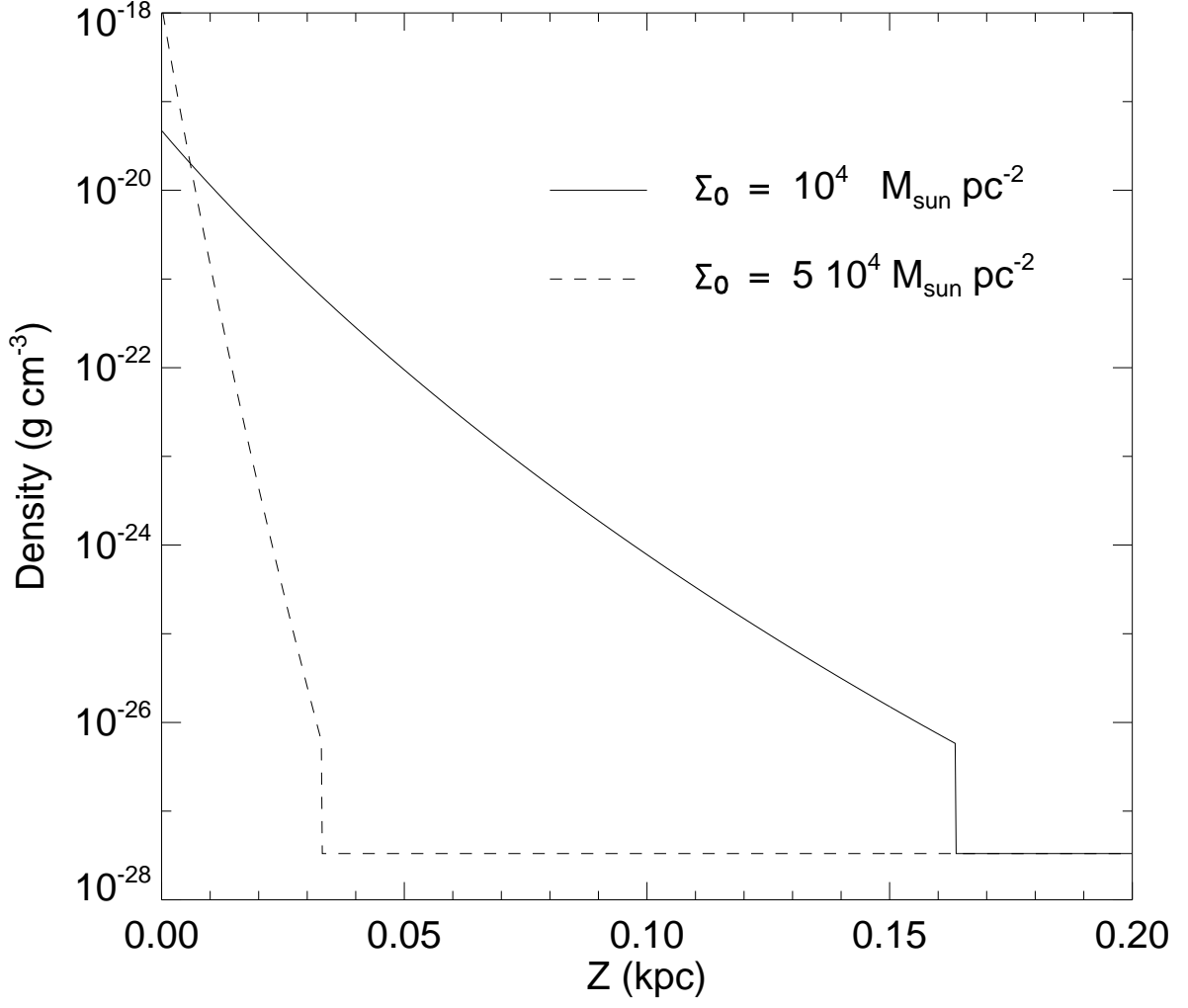


Fig. 1.— The density distributions of the disks with central surface densities of $\Sigma_0 = 10^4$ and $5 \times 10^4 \text{ M}_{\odot} \text{ pc}^{-1}$ in the vertical direction. The scale heights are $H = 7$ and 2 pc respectively.

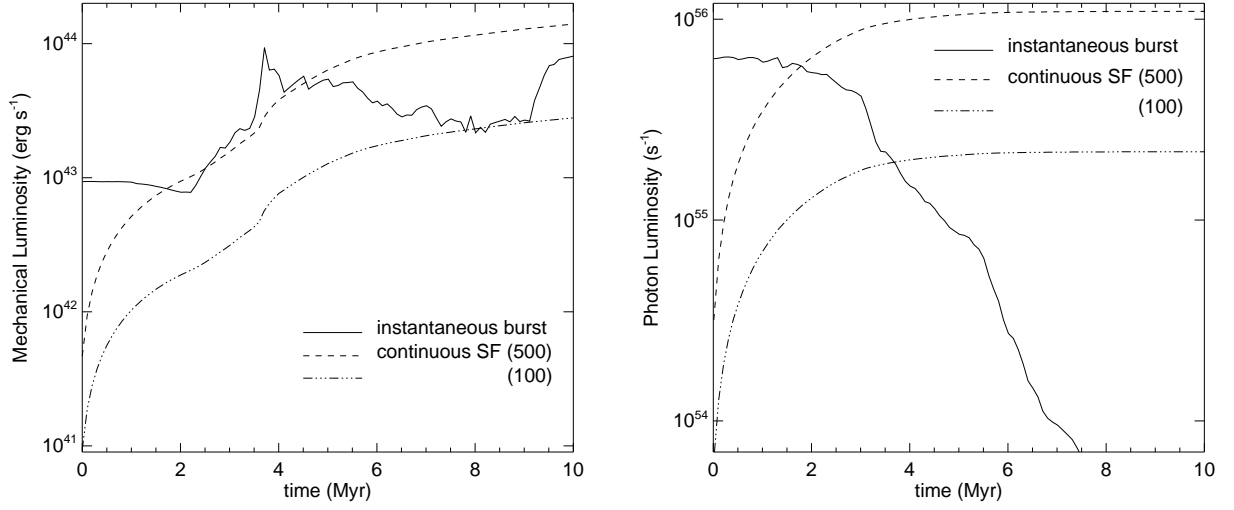


Fig. 2.— Mechanical luminosities (*left panel*) and ionizing photon luminosity (*right panel*) as a function of time for three starburst scenarios: instantaneous starburst with $M_* = 10^9 \text{ M}_{\odot}$ (*solid line*); continuous star formation with $500 \text{ M}_{\odot} \text{ yr}^{-1}$ (*dashed line*); and continuous star formation with $100 \text{ M}_{\odot} \text{ yr}^{-1}$ (*dash-dotted line*). Population synthesis models are from Starburst 99 (Leitherer et al. 1999).

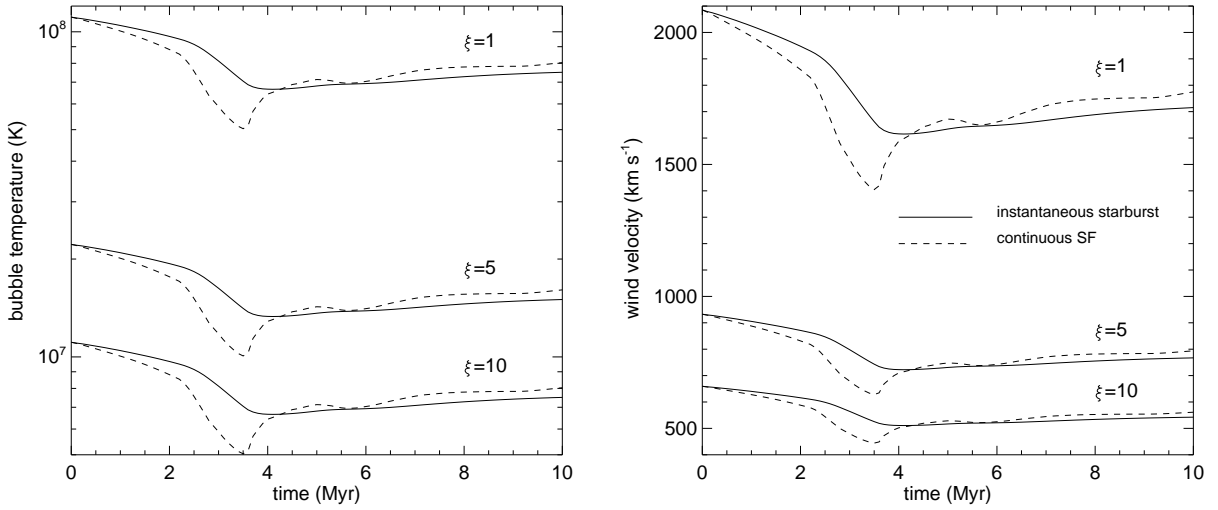


Fig. 3.— The (a) temperature of a hot bubble in a uniform medium driven by a starburst with L_{mech} and the rate of supernova ejecta $M_{\text{SN}} \propto L_{\text{mech}}$ predicted by the Starburst 99 model as a function of time, with the given mass-loading factors ξ , under the assumption of an instantaneous (*solid line*) or continuous (*dashed line*) starburst. The amount of mass in the hot wind is ξM_{SN} . (b) The expected terminal velocity of the wind driven by such a bubble after its blowout from a stratified disk. Note T_{wind} and v_{wind} are proportional to $L_{\text{mech}}/M_{\text{SN}}$, thus independent of SFR assumed.

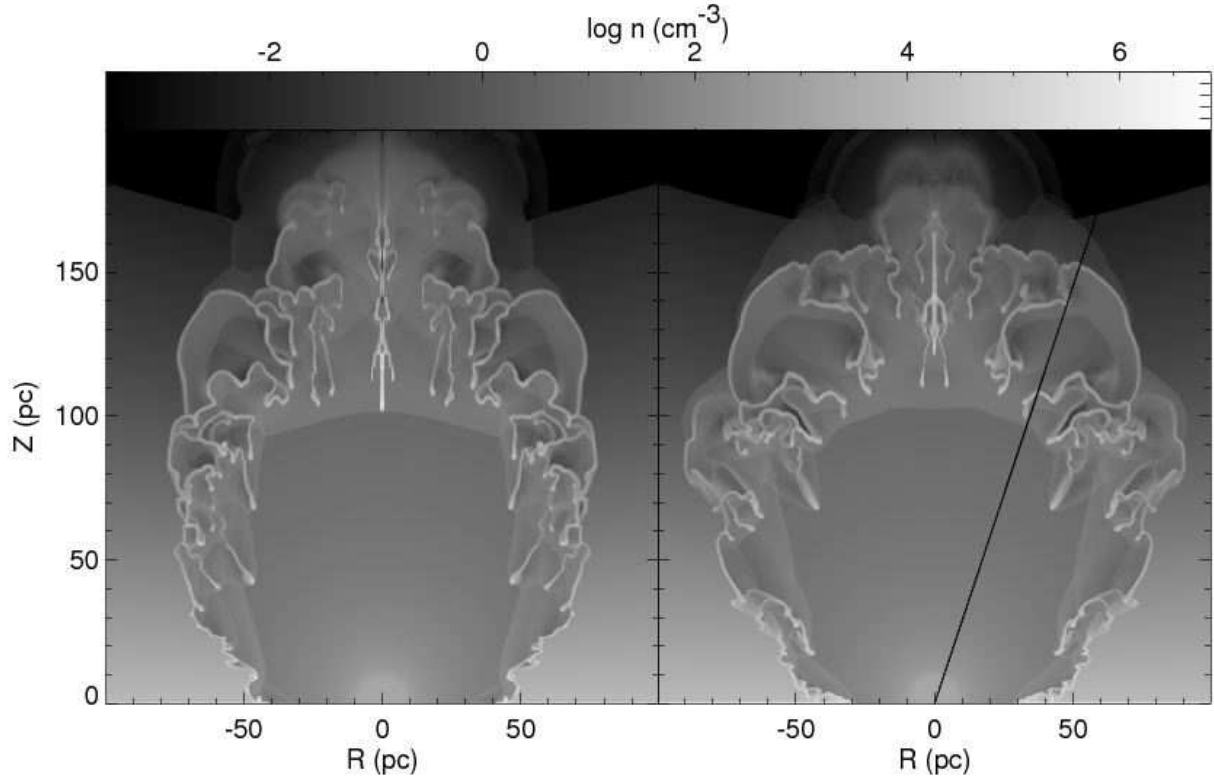


Fig. 4.— The density distributions of our standard model at $t = 0.27$ Myr with the cooling temperature cut-offs of $T_{\text{floor}} = 10^2$ (U1: *left panel*) and 10^4 K (X1: *right panel*) respectively. Note that because the shell remains underresolved, the temperature floor does not substantially influence the behavior of the shell in our models. The dark line denotes our fiducial line of sight.

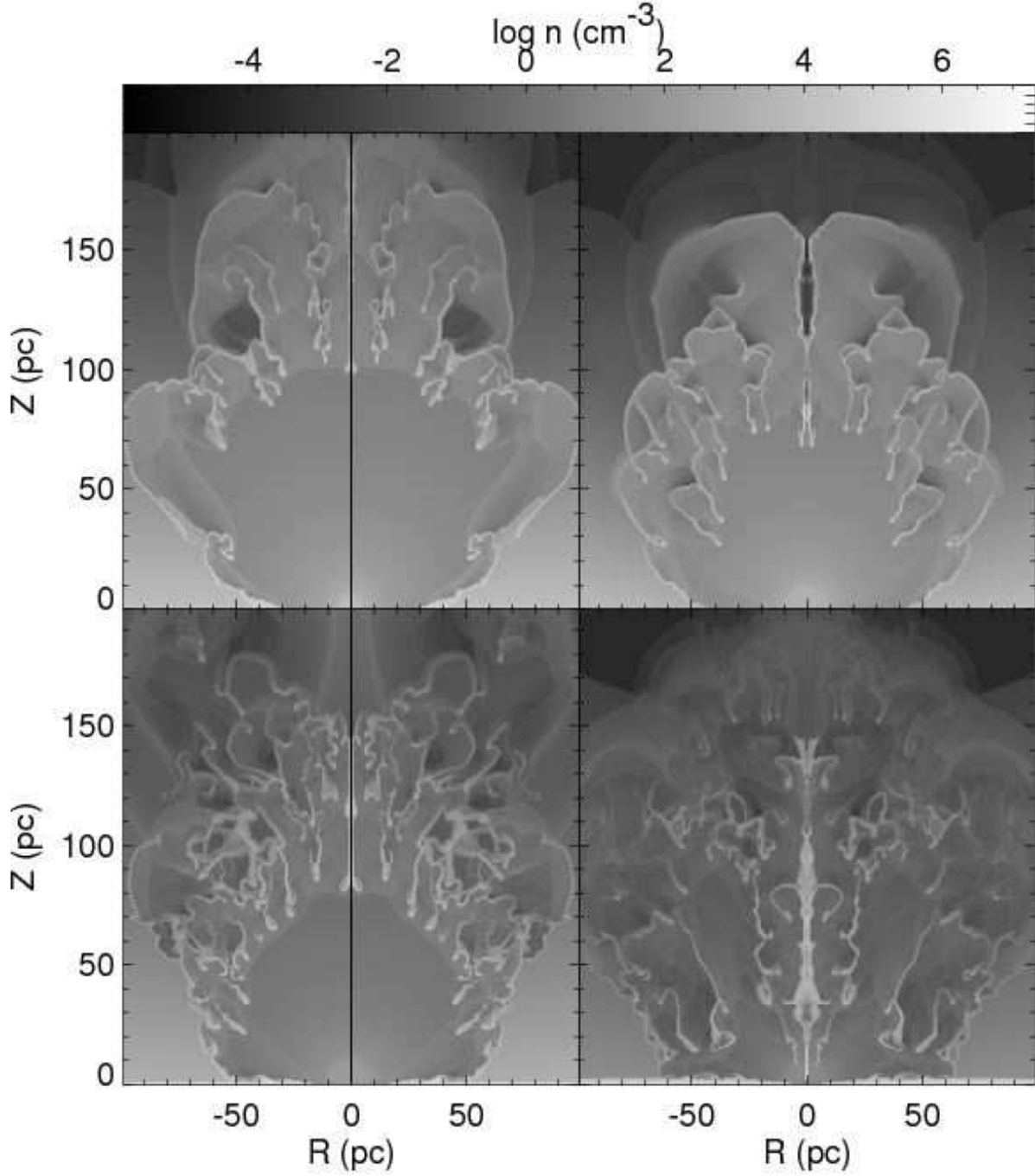


Fig. 5.— (*top*) The density distributions of two models with $L_{\text{mech}} = 10^{43} \text{ erg s}^{-1}$: (*top left*) our fiducial model with a source region of only 25 zones, model S1, and (*top right*) model V1 with a higher surface density $\Sigma_0 = 5 \times 10^4 \text{ M}_\odot \text{ pc}^{-2}$. (*bottom*) The density distributions of two models with lower mechanical luminosities: (*bottom left*) model X2 with $L_{\text{mech}} = 10^{42}$ and (*bottom right*) model X3 with $L_{\text{mech}} = 10^{41} \text{ erg s}^{-1}$. Each model is shown just before it exits the grid, at times of $t = 0.28, 0.22, 0.49,$ and 0.85 Myr respectively.

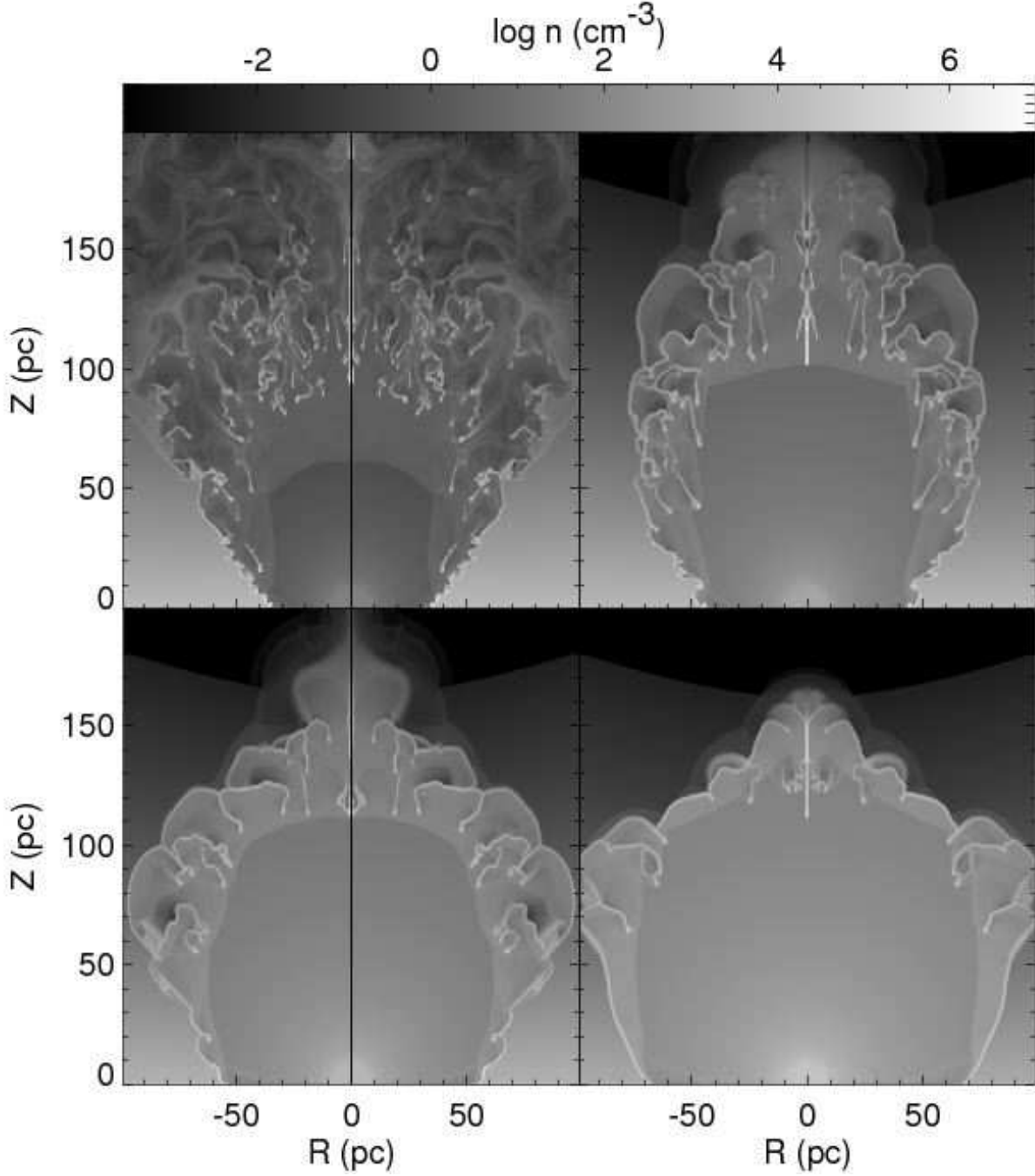


Fig. 6.— The density distributions of our model with $T_{\text{floor}} = 10^2$ K with different mass-loading rates: $\dot{M}_{\text{in}} = 1.7 \text{ M}_{\odot} \text{ yr}^{-1}$ (U1-A: *top left*), $17 \text{ M}_{\odot} \text{ yr}^{-1}$ (U1: *top right*), $49 \text{ M}_{\odot} \text{ yr}^{-1}$ (U1-B: *bottom left*), and $120 \text{ M}_{\odot} \text{ yr}^{-1}$ (U1-C: *bottom right*). They are shown at $t = 0.22, 0.27, 0.35$, and 0.41 Myr respectively. Different mass-loading rates correspond to different wind temperatures and terminal wind velocities. Note that the growth of hydrodynamic instabilities is suppressed as the mass-loading rate decreases and the terminal wind velocity increases.

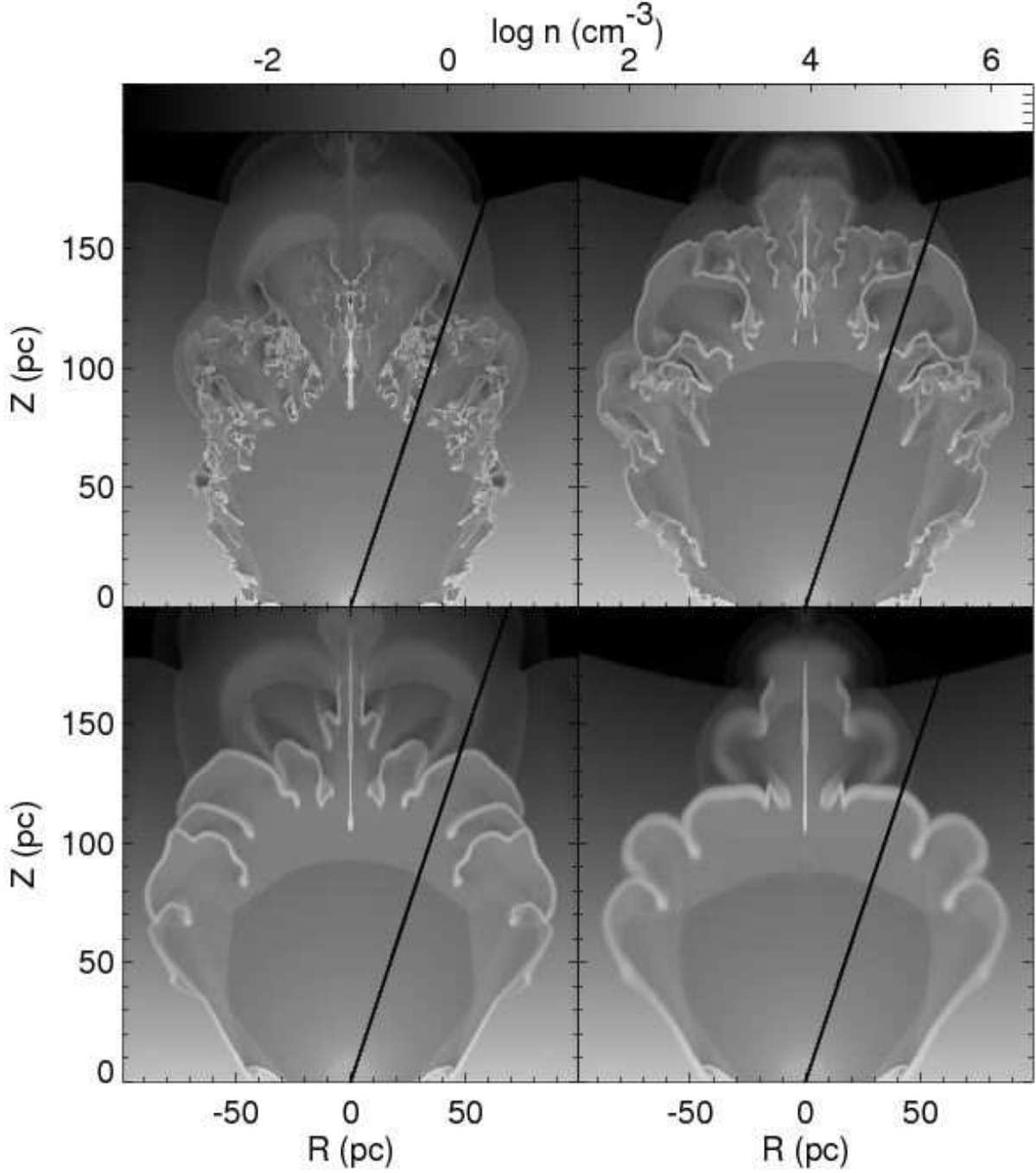


Fig. 7.— The density distributions of our standard model with $T_{\text{floor}} = 10^4$ K at $t = 0.27$ Myr, with resolution of 0.1 pc (X1-0: *top left*), our fiducial resolution of 0.2 pc (X1: *top right*), and resolutions of 0.4 pc (X1-2: *bottom left*) and 0.8 pc (X1-4: *bottom right*). Note that the growth of R-T instability is suppressed as the resolution decreases. The black lines show the typical line of sight used for line profile analysis.

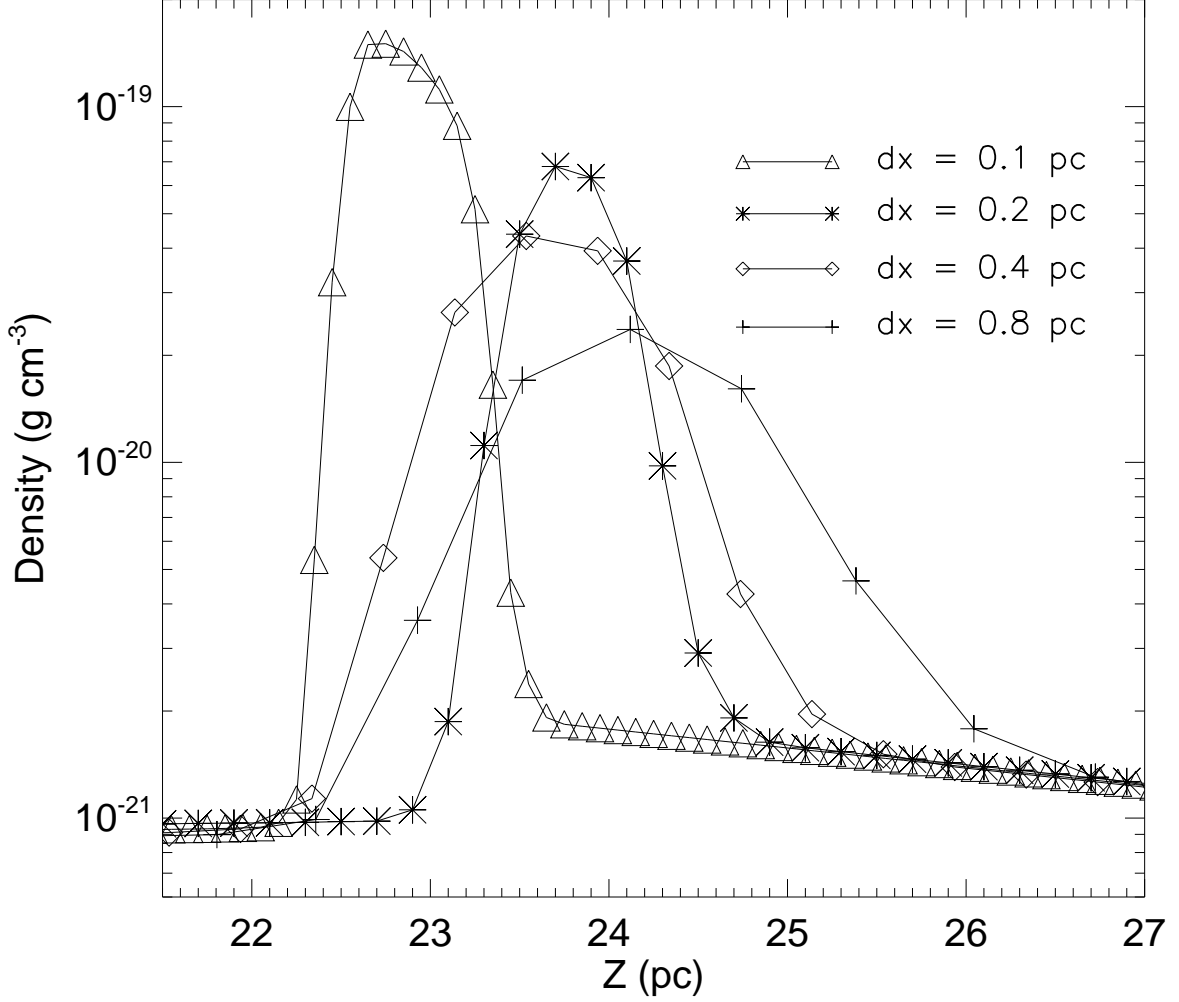


Fig. 8.— Density profiles at the outer shock fronts in the vertical direction at $t = 0.06$ Myr for 0.1 pc resolution (*triangles*; model X1-0), and at $t = 0.05$ Myr for 0.2 pc (*stars*; X1), 0.4 pc (*diamonds*; X1-2), and 0.8 pc (*crosses*; X1-4) resolution. The shell is better resolved with a higher resolution, but still not fully resolved even at 0.1 pc resolution. (Note that the size of the highest resolution bubble is slightly smaller only because of the smaller source region.)

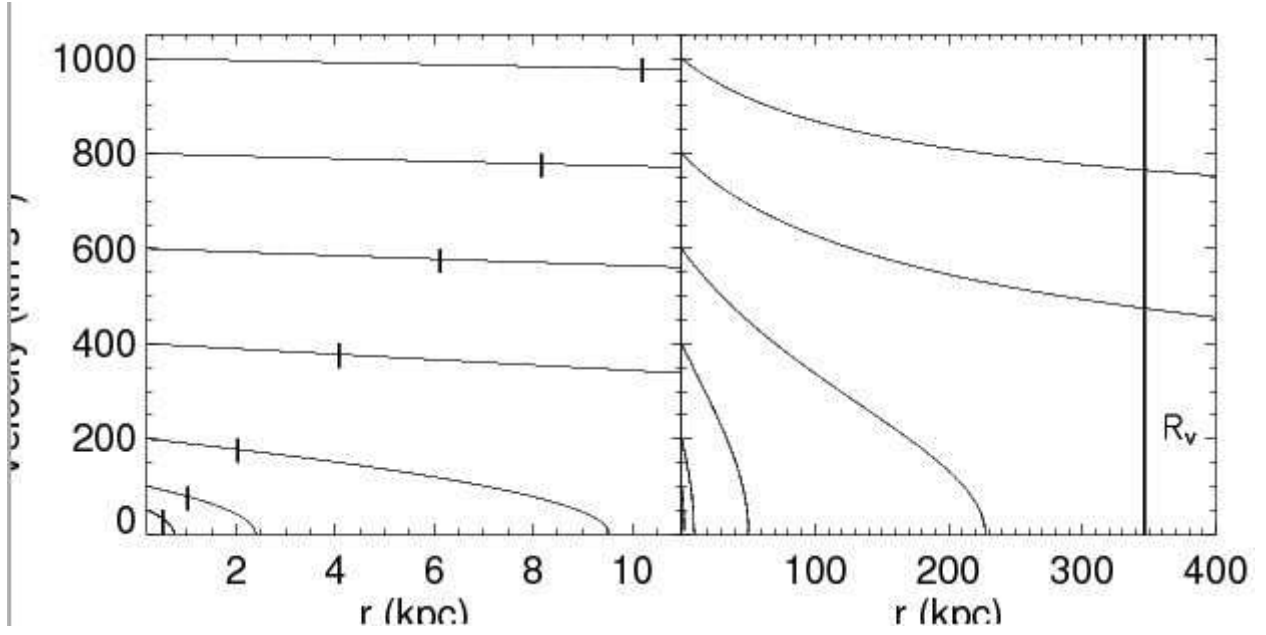


Fig. 9.— The velocity predicted by the ballistic approximation for shell fragments as they expand radially in the halo from $r_b = 0.2$ kpc with initial (blowout) velocities, $v_b = 50, 100, 200, 400, 600, 800$, and 1000 km s^{-1} . The *left* panel shows the behavior near the galaxy, while the *right* panel captures the full extent of the halo. Radii at $t = 10$ Myr (*left panel*) and the virial radius (*right panel*) are noted with *thick lines*.

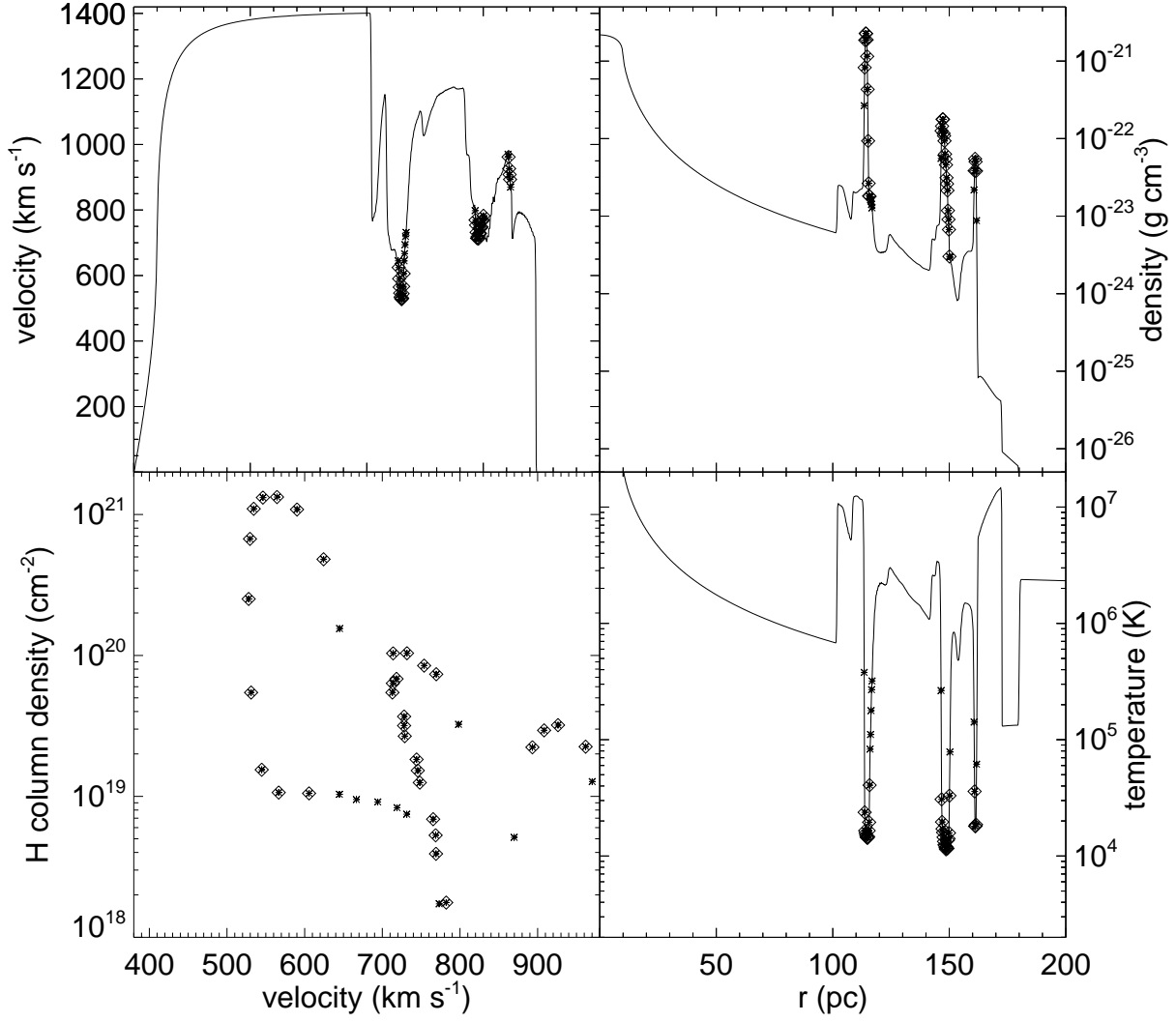


Fig. 10.— The radial velocity (*top left*), the density (*top right*), and the temperature (*bottom right*) distributions of gas along a line of sight through the center at an angle of 19° from the vertical axis in model X1 at the end of the simulation. Regions of cold gas with $T < 5 \times 10^4$ K (which we take to be Na I absorbing gas) are shown in *diamonds*. In the *bottom left* panel, the distribution of column density for the cold gas as a function of radial velocity is plotted.

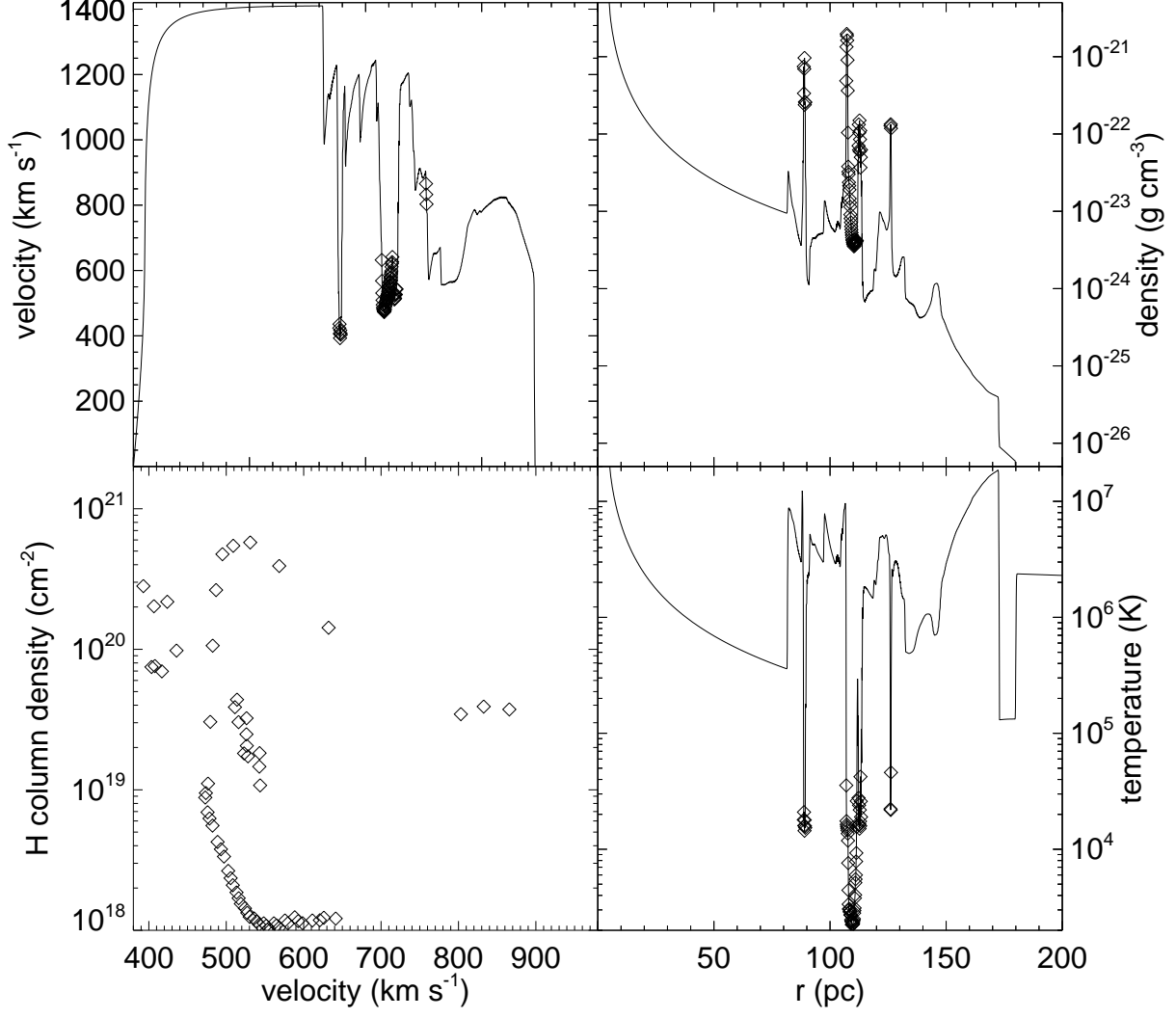


Fig. 11.— The same as in Figure 10 for the same standard simulation, but with our highest resolution of 0.1 pc (X1-0).

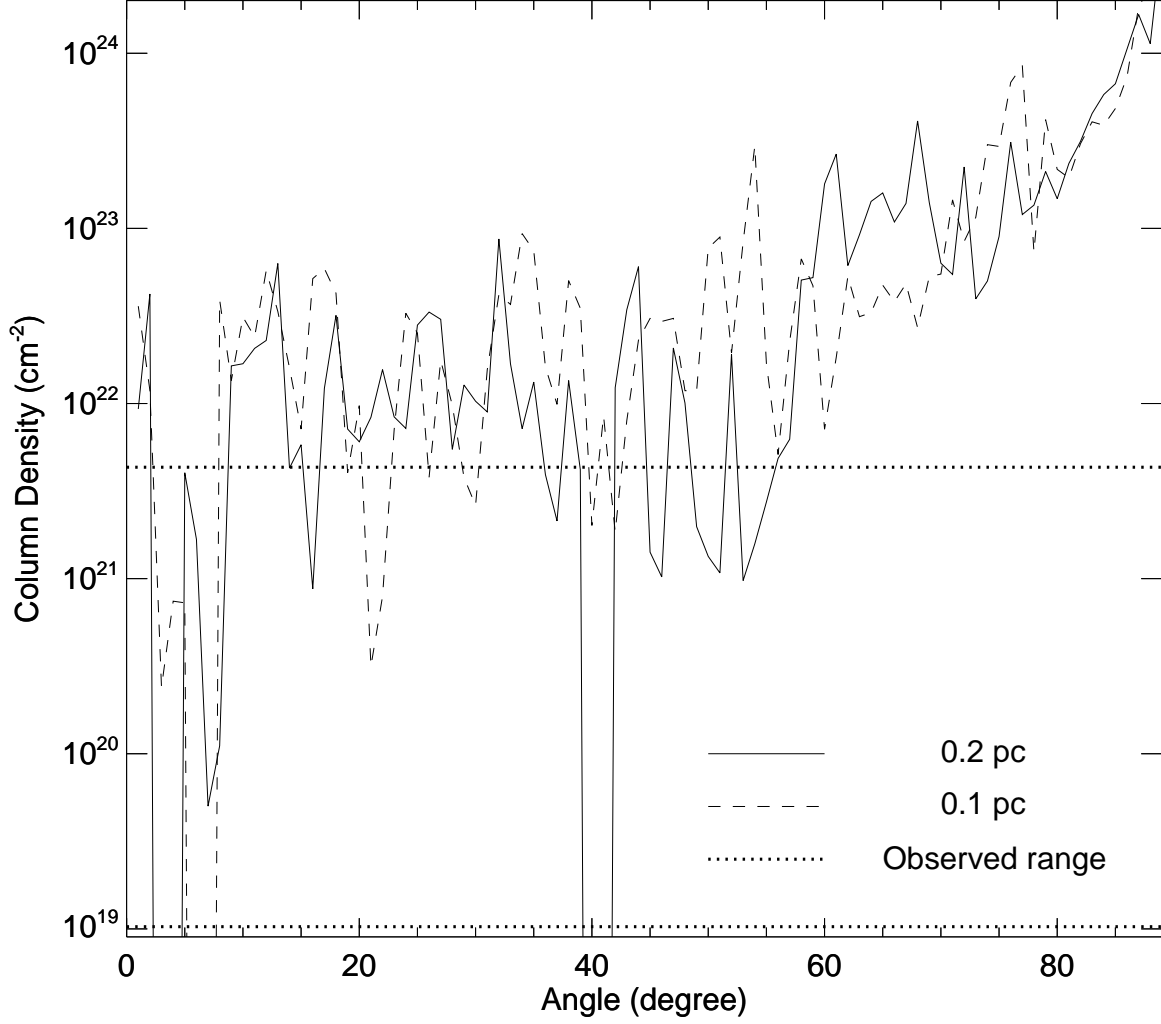


Fig. 12.— The column density distributions of cool gas at sightlines through the center as a function of angle extended from the vertical axis in models with 0.2 pc (*solid line*; model X1) and 0.1 pc (*dashed line*; X1-0) resolution. The observed range of column density inferred from observations of Na I absorption profiles is $1.0 \times 10^{19} - 4.3 \times 10^{21} \text{ cm}^{-2}$, shown in *dotted lines*. Note that the column densities from the models will be reduced over time due to spherical expansion.

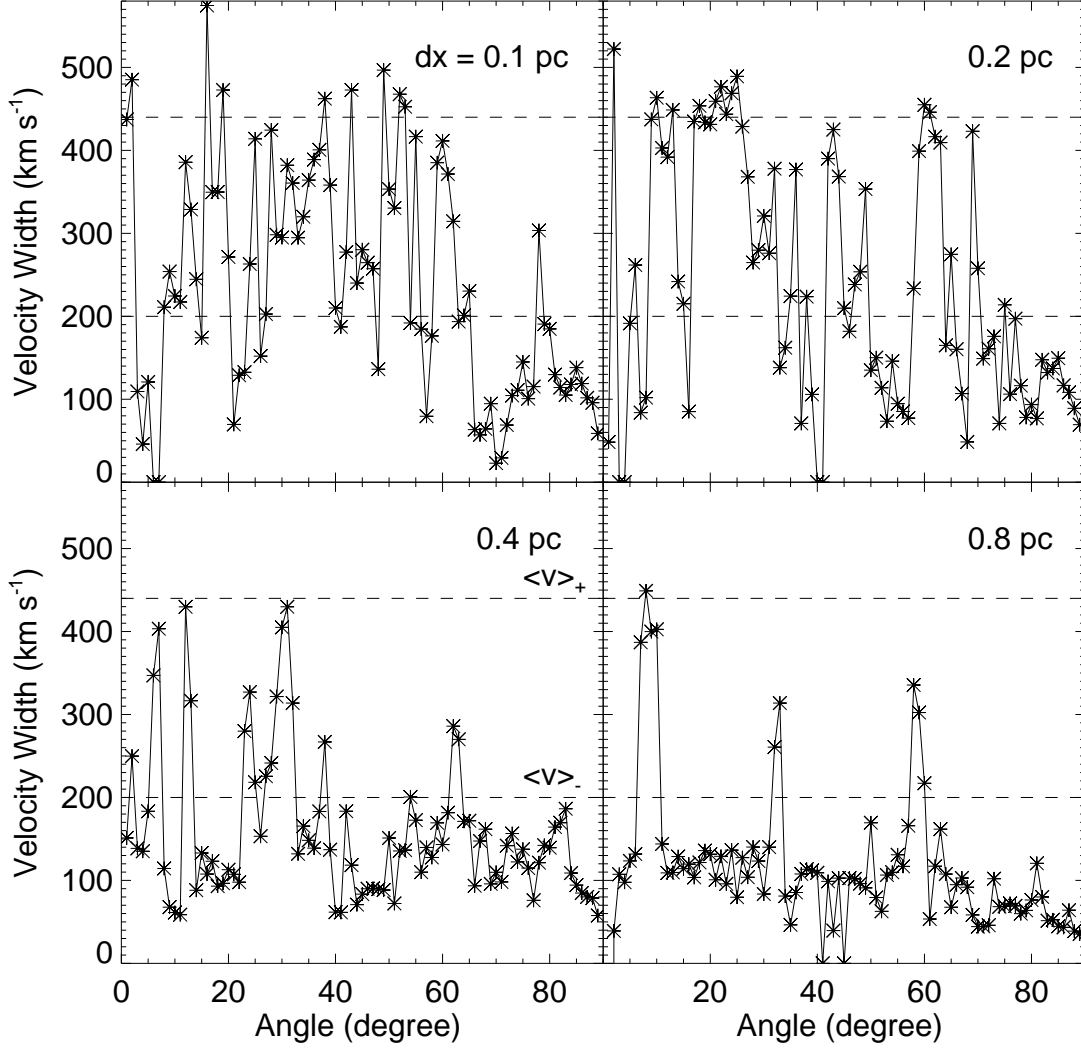


Fig. 13.— The velocity widths are shown as a function of angle from the vertical axis at every degree for models with grid resolutions of $dx = 0.1, 0.2, 0.4$, and 0.8 pc (models X1-0, X1, X1-2, and X1-4). Note that the highest two resolutions appear to display converged behavior. The upper and lower limits of the observed average line width in Na I absorption are shown in (*dashed lines*): $\langle v \rangle = 320 \pm 120$ km s⁻¹.

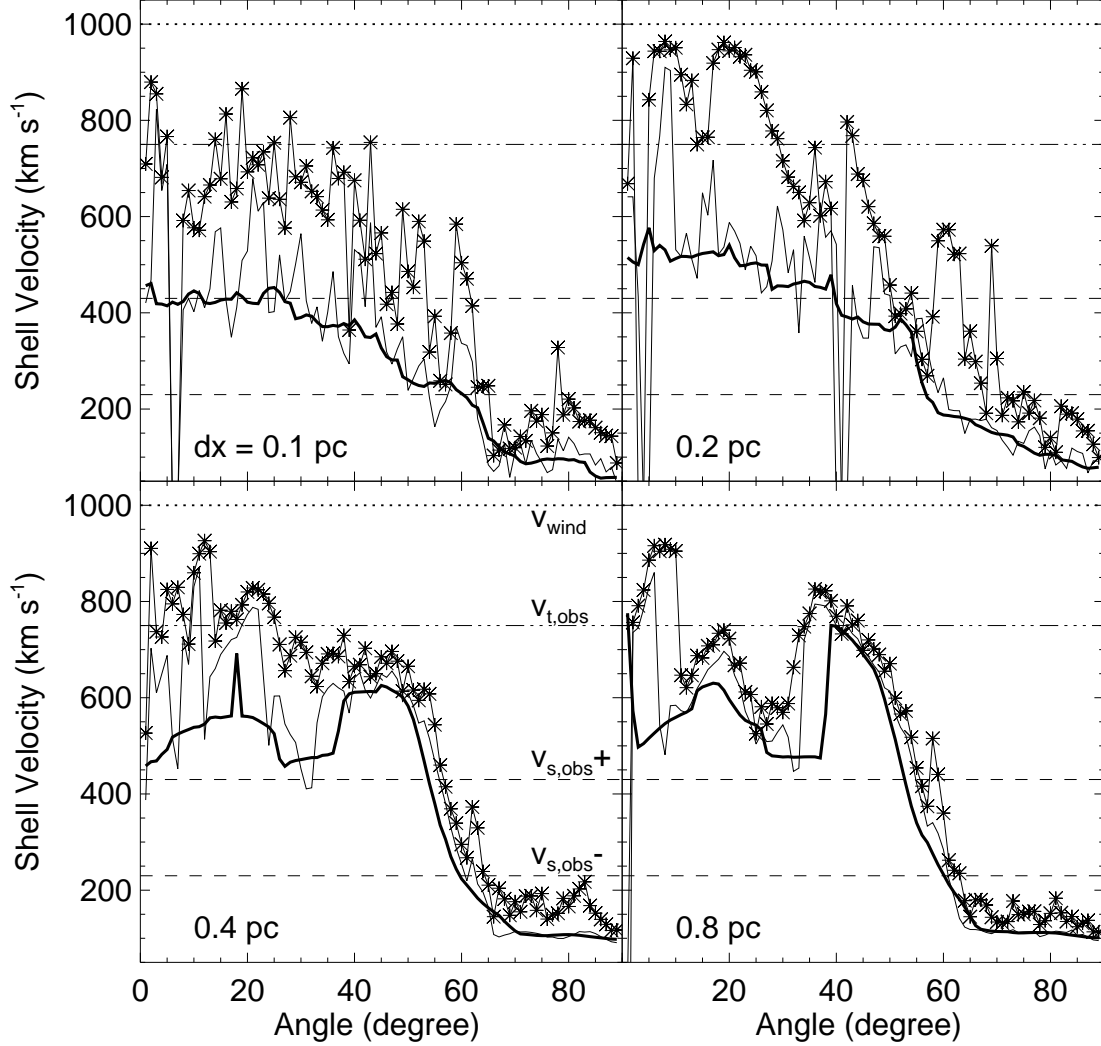


Fig. 14.— The terminal velocity (*solid line with asterisks*) and the average mass-weighted velocity (*thin solid line*) of cool gas are plotted as a function of angle from the vertical axis along sightlines through the galactic center in models with grid resolutions of $dx = 0.1, 0.2, 0.4$, and 0.8 pc (models X1-0, X1, X1-2, and X1-4). Since shell mass varies substantially with angle, we also plot the mass-weighted average velocity within a 10° arc $v_{av,10}$ at each angle (*thick solid line*). We show the terminal velocity of the low density wind $v_{wind} \approx 1000$ km s⁻¹ in *dotted line*, the observed average shell velocity $v_{s,obs} = 330 \pm 100$ km s⁻¹ in *dashed line*, and the observed average terminal velocity $v_{t,obs} = 750$ km s⁻¹ in *dash-dot-dot line*.

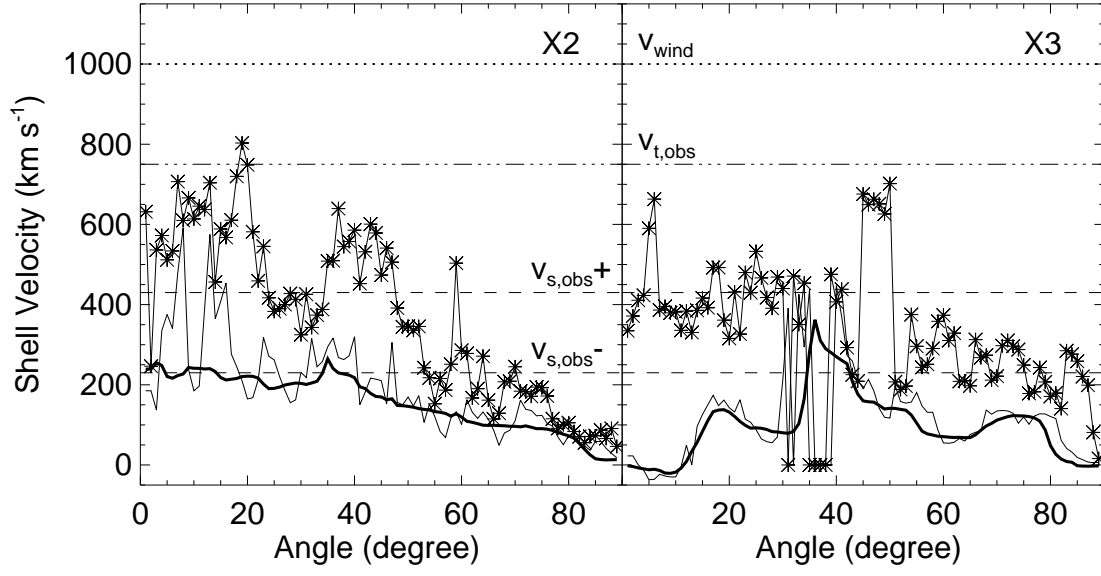


Fig. 15.— Same as in Figure 14 for lower luminosity runs with $L_{\text{mech}} = 10^{41} \text{ erg s}^{-1}$ (*right*; model X3), and $10^{42} \text{ erg s}^{-1}$ (*left*; X2).

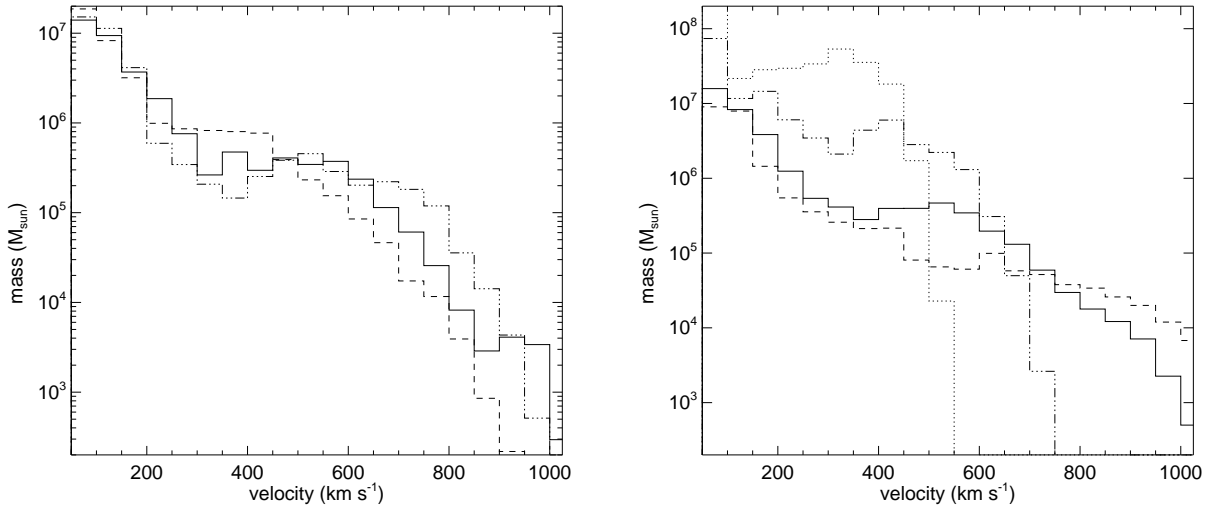


Fig. 16.— The mass distribution of all the cool shells and shell fragments as a function of velocity for (a) models at $t = 0.27$ Myr with increasing zone sizes $dx = 0.1$ pc (*dashed line*; model X1-0), 0.2 pc (*solid line*; X1), and 0.4 pc (*dashed-dot-dot line*; X1-2), and (b) models at the blowout time ($t = 0.22, 0.27, 0.33$, and 0.41 Myr) with increasing mass loading of the wind $1.7 M_{\odot} \text{ yr}^{-1}$ (*dashed line*; model U1-A), $17 M_{\odot} \text{ yr}^{-1}$ (*solid lines*; U1), $49 M_{\odot} \text{ yr}^{-1}$ (*dashed-dot-dot line*; U1-B), and $120 M_{\odot} \text{ yr}^{-1}$ (*dotted line*; U1-C.).

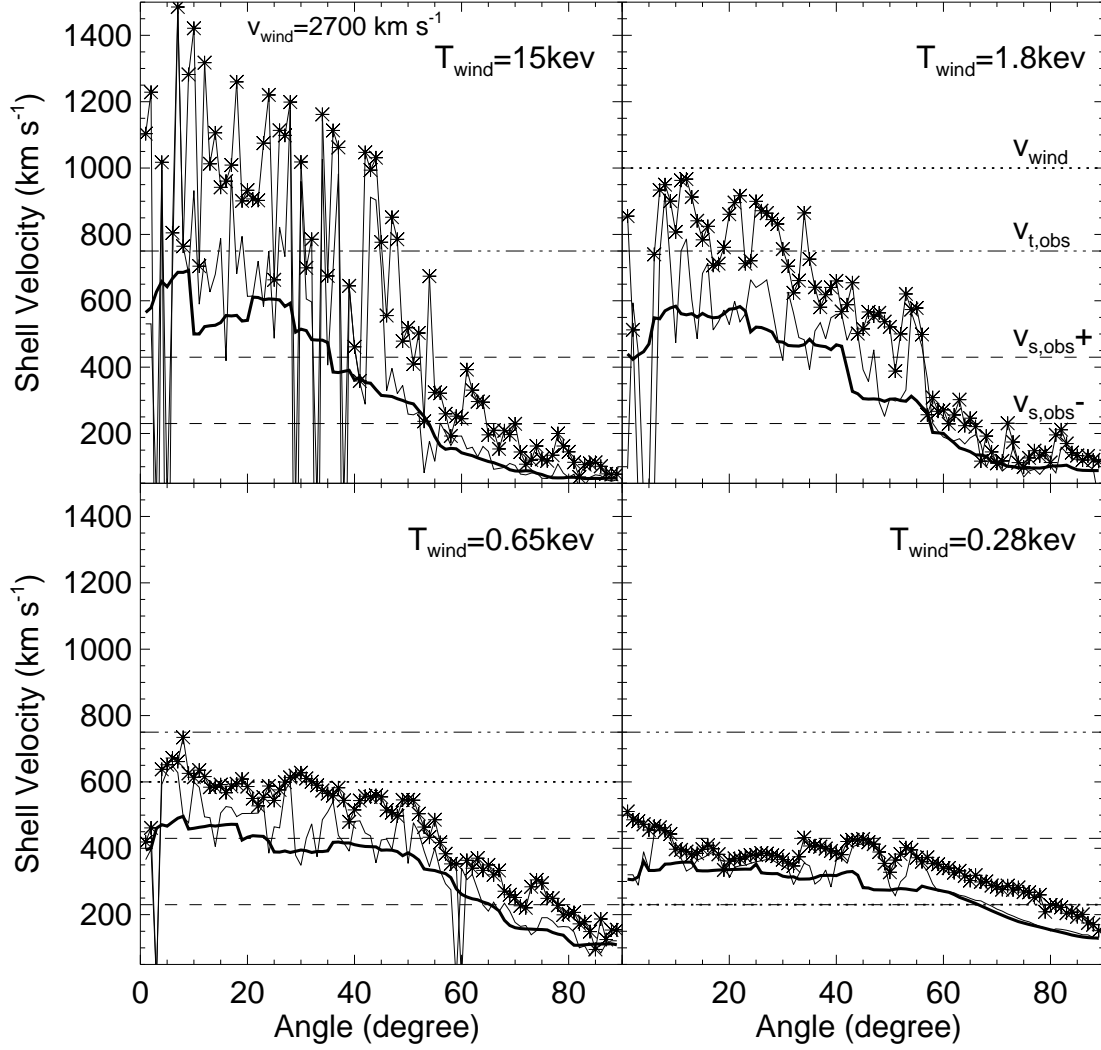


Fig. 17.— Same as in Figure 14 for models with increasing mass-loading of the wind $1.7 \text{ M}_{\odot} \text{ yr}^{-1}$ (top left; model U1-A) at $t = 0.22 \text{ Myr}$, $17 \text{ M}_{\odot} \text{ yr}^{-1}$ (top right; U1) at $t = 0.27 \text{ Myr}$, $49 \text{ M}_{\odot} \text{ yr}^{-1}$ (bottom left; U1-B) at $t = 0.35 \text{ Myr}$, and $120 \text{ M}_{\odot} \text{ yr}^{-1}$ (bottom right; U1-C) at $t = 0.41 \text{ Myr}$.

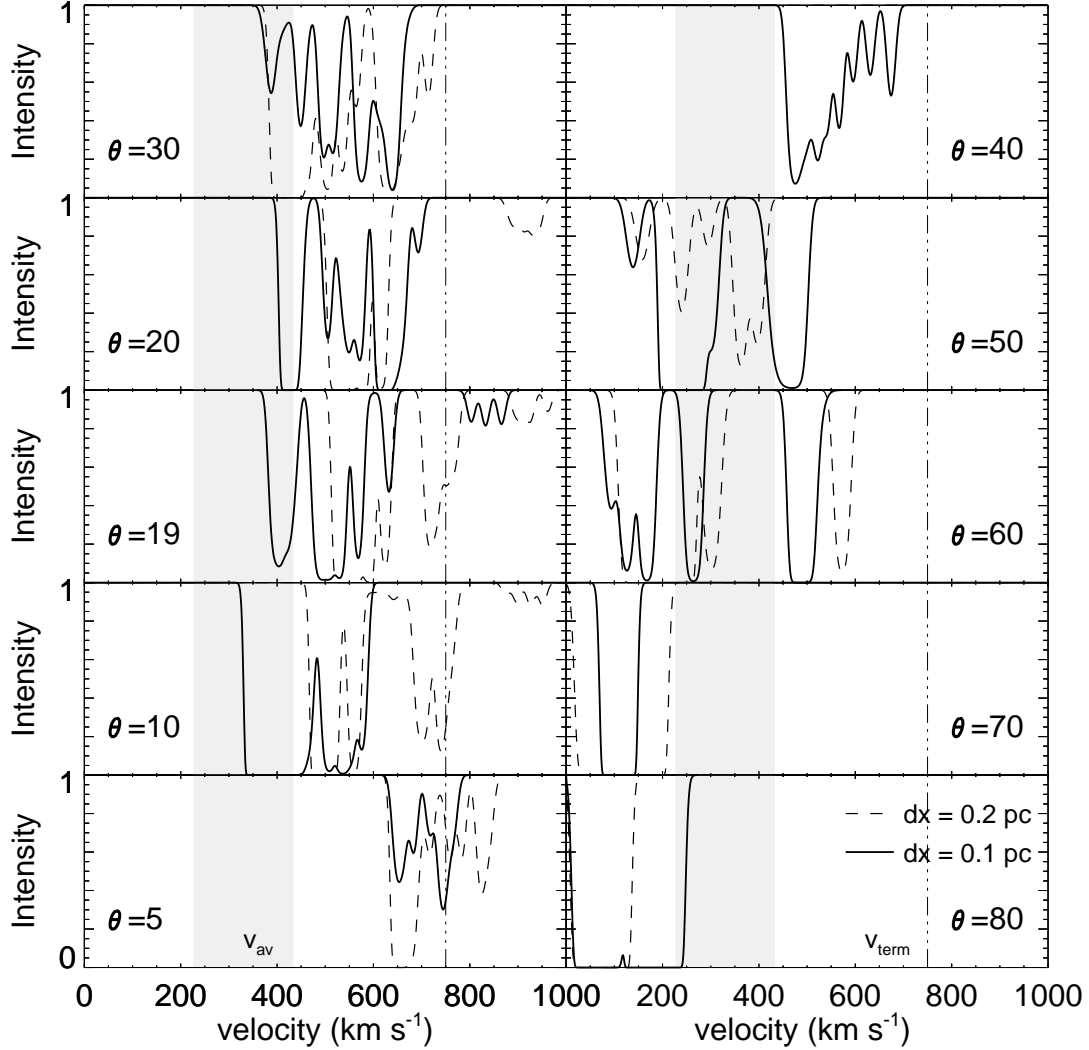


Fig. 18.— Simulated Na I 5890 absorption profiles at sightlines $\theta = 5^\circ, 10^\circ, 19^\circ, 20^\circ, 30^\circ, 40^\circ, 50^\circ, 60^\circ, 70^\circ$, and 80° (clockwise from the bottom left) for models with $dx = 0.1$ pc (solid line; model X1-0) and 0.2 pc (dashed line; X1). We also show the observed range of average shell velocity in shaded area and the observed average terminal velocity in dash-dot-dot line.

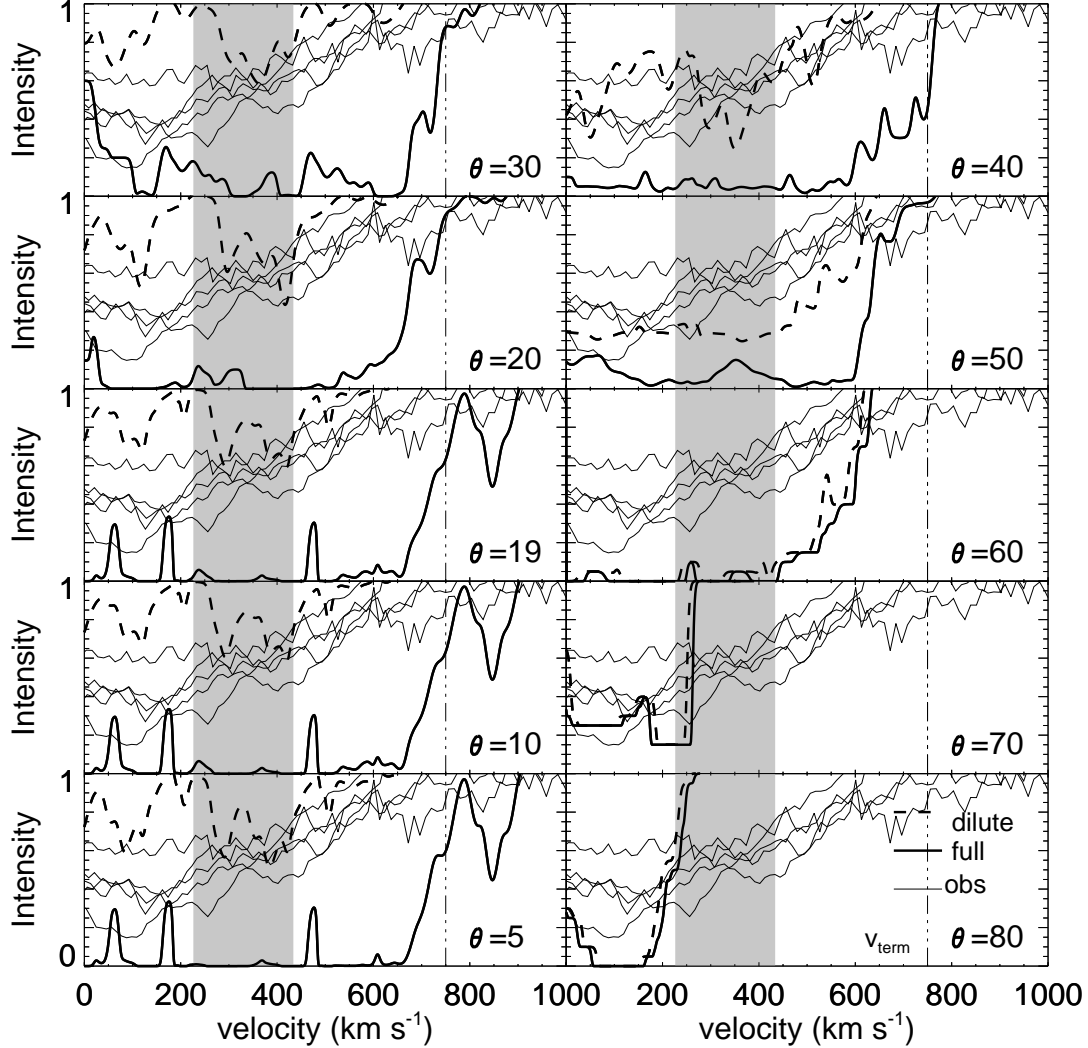


Fig. 19.— Simulated Na I 5890/5896 doublet absorption profiles averaged over 20° centered on the given (non-uniformly distributed) angles for model X1-0 with $dx = 0.1$ pc (*solid line*). The same profiles are shown after geometric dilution by a factor of 100 (*dashed line*), for comparison with five observed ULIRG spectra (*thin solid lines*) from Martin (2005). Note that the velocity frame is centered on the 5890 line; blue-shifted absorption from the 5896 line lies at low velocities in this frame. We also show the observed range of average shell velocity in *shaded area* and the observed average terminal velocity in *dash-dot-dot line*.

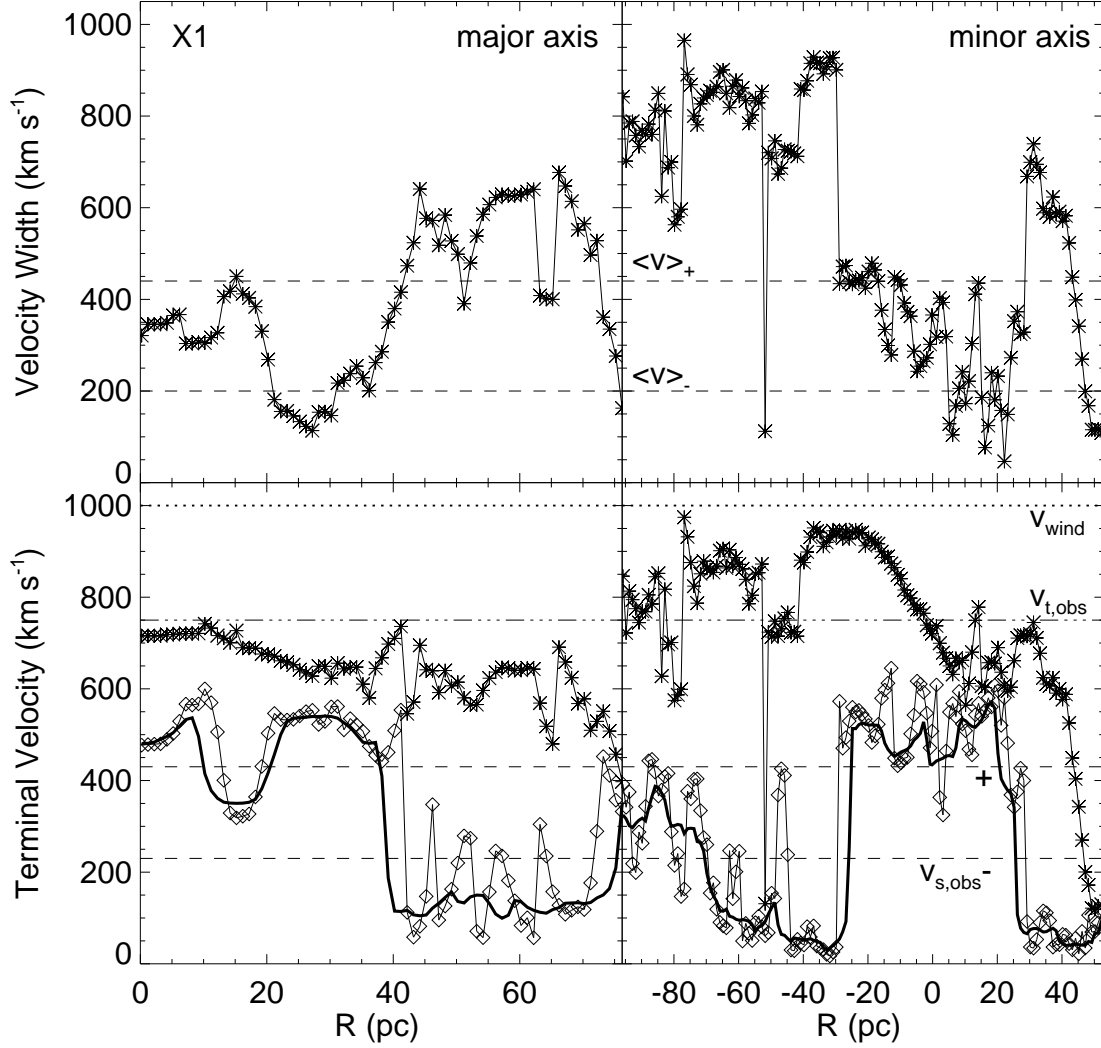


Fig. 20.— The velocity width is plotted as in Figure 13 (*top panels*), and the mass-weighted average velocity and the terminal velocity are plotted as in Figure 14 (*bottom panels*) for model X1. Parallel sightlines are chosen along a slit oriented at $\theta = 30^\circ$ from the axisymmetric axis and the major axis (*left panels*) and the minor axis (*right panels*).

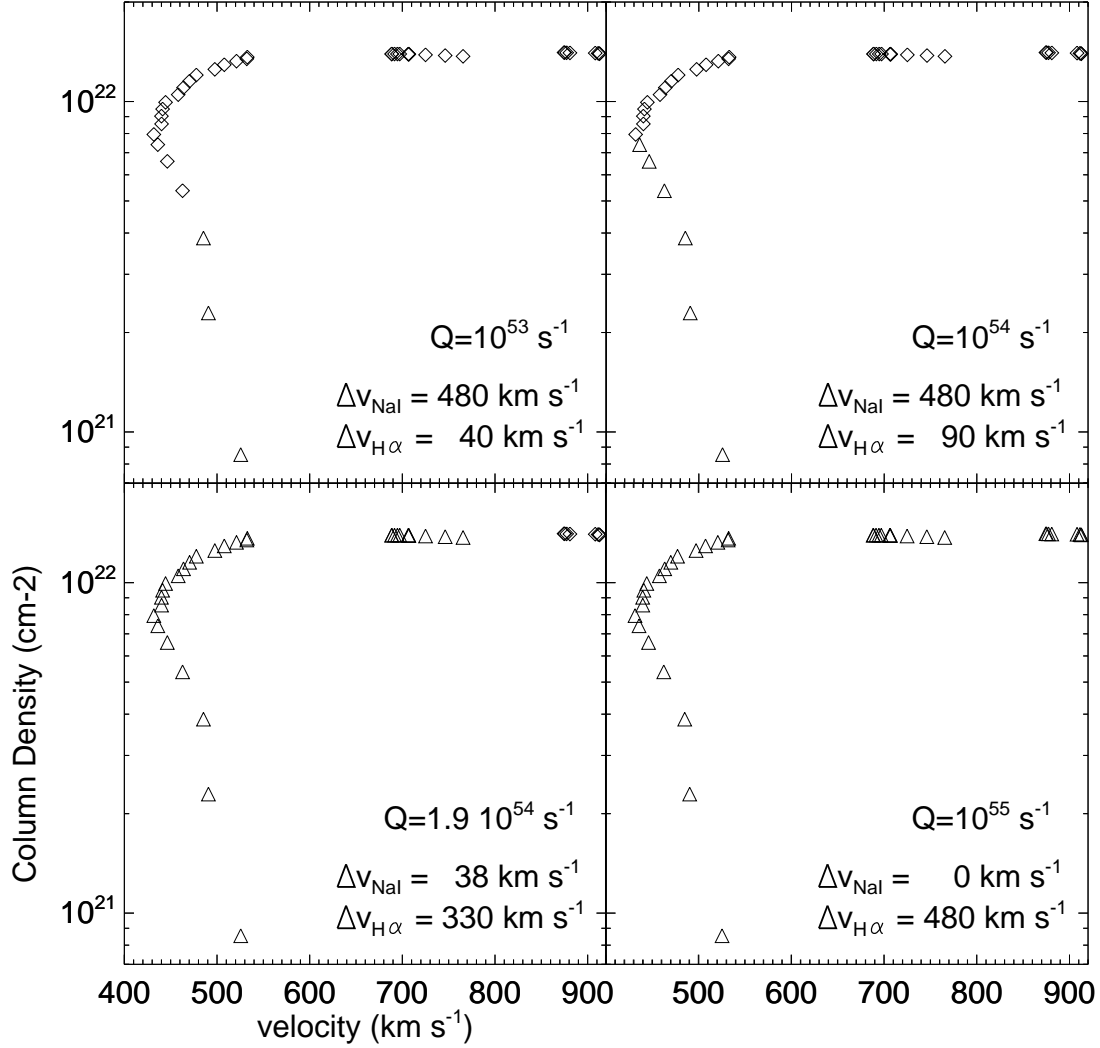


Fig. 21.— The column density distributions as a function of radial velocity for Na I absorbing gas (*diamonds*) and H α emitting gas (*triangles*) with photon luminosities of $Q = 10^{53}$, 10^{54} , 1.9×10^{54} , and 10^{55} photons s⁻¹ in a line of sight through the center at an angle of 13° from the vertical axis in model U1. The velocity widths of the two components vary as Q is changed.

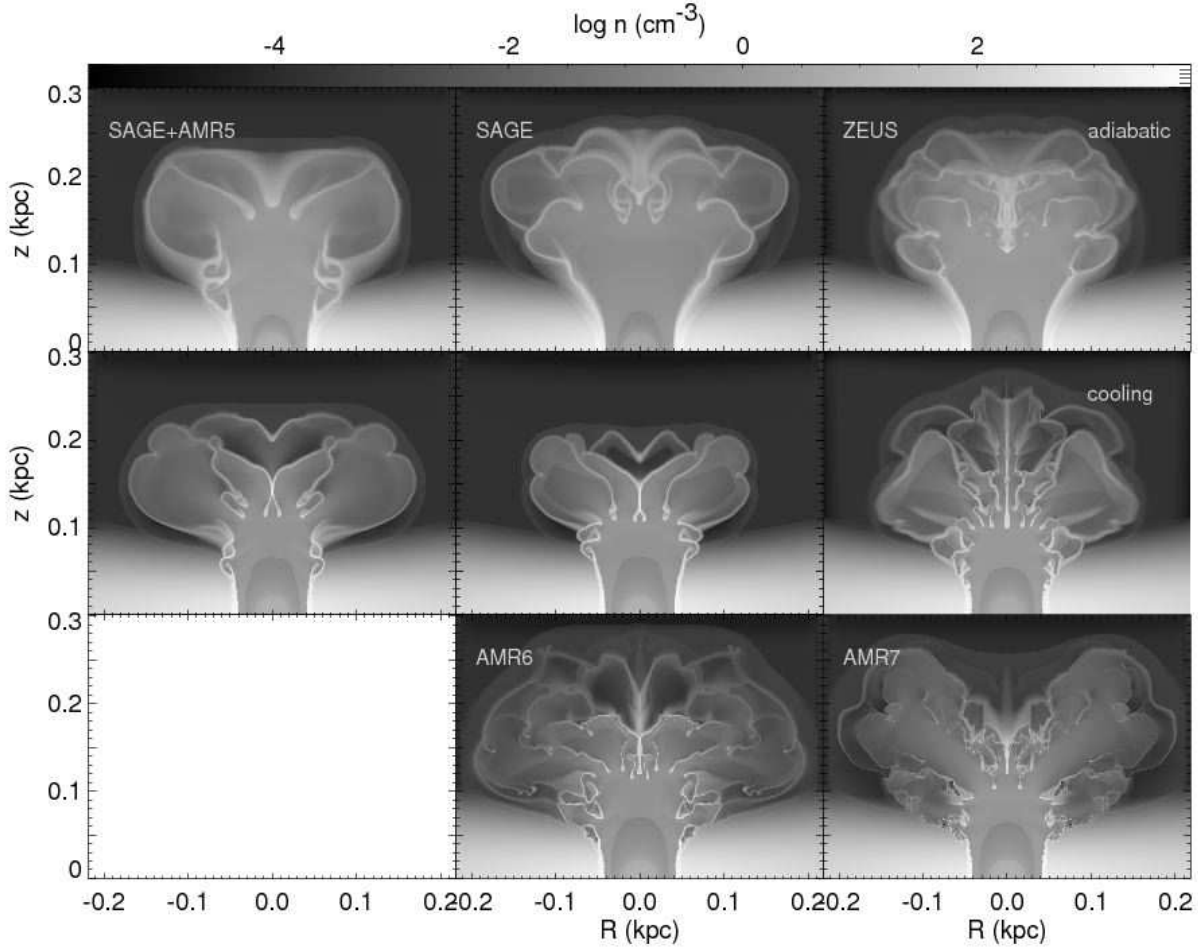


Fig. 22.— The density distributions at blowout in our model dwarf galaxy with $M_d = 10^8 M_\odot$ and $L_{\text{mech}} = 10^{40} \text{ erg s}^{-1}$ at $z = 8$. The bubbles are shown at the time of blowout. This is $t = 1$ Myr for models without radiative cooling, $t = 1.3$ Myr for SAGE models with radiative cooling, and $t = 1.1$ Myr for ZEUS-3D models. The top row shows models without radiative cooling using SAGE with uniform grid and 5 levels of AMR, and using ZEUS-3D. These are models AN, UN, and RN. The middle row shows the same grids with radiative cooling, models AC, UC, and RC. Finally, the bottom row shows SAGE models with cooling and 6 and 7 levels of AMR, models BC, and CC.